



UNIVERSIDAD DE INVESTIGACIÓN DE TECNOLOGÍA EXPERIMENTAL YACHAY

Escuela de Ciencias Químicas e Ingeniería

CO₂ CAPTURE BY CLAY MEMBRANE WITH METAL OXIDE NANOPARTICLES

Trabajo de integración curricular presentado como requisito para la obtención
del título de Químico.

Autor:

Oscar Raúl Almeida Molina

Tutor:

Edward Ebner Ávila Sosa, Ph.D.

Co-Tutor:

Marvin José Ricaurte Fernández, Ph.D.

Urcuquí, Enero 2025

AUTORÍA

Yo, **OSCAR RAUL ALMEIDA MOLINA**, con cédula de identidad 1721630604, declaro que las ideas, juicios, valoraciones, interpretaciones, consultas bibliográficas, definiciones y conceptualizaciones expuestas en el presente trabajo; así cómo, los procedimientos y herramientas utilizadas en la investigación, son de absoluta responsabilidad de el/la autora (a) del trabajo de integración curricular. Así mismo, me acojo a los reglamentos internos de la Universidad de Investigación de Tecnología Experimental Yachay.

Urcuquí, Enero 2025.

Oscar Raul Almeida Molina
CI:1721630604

AUTORIZACIÓN DE PUBLICACIÓN

Yo, ALMEIDA MOLINA OSCAR RAUL, con cédula de identidad 1721630604, cedo a la Universidad de Investigación de Tecnología Experimental Yachay, los derechos de publicación de la presente obra, sin que deba haber un reconocimiento económico por este concepto. Declaro además que el texto del presente trabajo de titulación no podrá ser cedido a ninguna empresa editorial para su publicación u otros fines, sin contar previamente con la autorización escrita de la Universidad.

Asimismo, autorizo a la Universidad que realice la digitalización y publicación de este trabajo de integración curricular en el repositorio virtual, de conformidad a lo dispuesto en el Art. 144 de la Ley Orgánica de Educación Superior

Urququí, Enero 2025.

Oscar Raul Almeida Molina
CI: 1721630604

Acknowledgments

There are many people to acknowledge who've stayed in the most difficult moments to reach my objective. First, I want to thank my family for all the support they have given these years, especially my parents, who never abandoned me and gave me the strength and motivation until the end. My siblings, who always took care, and their sincere words of encouragement.

Thanks to my second family in Yachay, who gave their friendship, affection, unforgettable moments, and experiences. Therefore, I want to thank Sebas, Jimmy, Juan Diego, Luis, Milena, Elaine, and Saul for being with me since the beginning of this adventure and giving their unconditional support whenever I need it. I would also like to express my gratitude to the people I met along the way: Alejandro, Nicole, Camila, and Emilio, with whom I shared great moments that I will always remember. Besides, a special mention to the person who has been the most patient, who was always there with advice and endangered me, but who never left me alone. Thanks for all, Veronica. I couldn't have it without you. Finally, I want to thank Alexia, who gave me the emotional support I needed to finish my thesis. Without her, I could not have written these acknowledgments for all of you.

There is a person who has been there almost all my academic life who did not let me give up when I wanted to leave everything. I am very fond, and without her, my life at the University would not have been the same. So, thanks to Deynna for helping me grow as a person and supporting me in everything I did over the years.

I thank each of my professors for giving me all the knowledge to become a professional. Above all, I thank my co-tutor, Marvin Ricaurte, and tutor, Edward Avila, who helped throughout this process and were always there to teach me whenever I had a doubt. Thus, this thesis was possible thanks to all of you.

Resumen

Actualmente, el dióxido de carbono (CO_2) es el mayor contribuyente al efecto invernadero, responsable del 75% del total de gases liberados a la atmósfera. Por lo tanto, se han desarrollado nuevos materiales y tecnologías para mitigar los efectos nocivos de este gas ácido. Una de estas alternativas es la captura de CO_2 , que usa materiales que están en constante desarrollo. Así, este estudio se centra en el desarrollo de membranas a base de arcillas de las provincias de Morona Santiago (COL-307) y Zamora Chinchipe (CZP-303) en Ecuador. Estas arcillas tuvieron un proceso de purificación para eliminar impurezas. Además, se les añadieron diferentes cantidades de óxido de zinc (ZnO), óxido de hierro como ilmenita (FeTiO_3) y magnesioferrita (MgFe_2O_4), y nanotubos de carbono (NTC) para mejorar la capacidad de adsorción de la arcilla. Las arcillas purificadas están compuestas de caolinita, que tiene una estructura porosa. La cual permite que los gases pasen a través de la membrana fácilmente, esto permite que el CO_2 tenga más sitios activos para adherirse y separar este gas de otros. Por lo tanto, se desarrollaron cilindros y esferas de arcilla con nanopartículas de ZnO , FeTiO_3 , MgFe_2O_4 y NTC. Los composites se probaron en un reactor de alta presión con CO_2 puro a 25°C . Esto para determinar la cantidad de moles de gas adsorbidos debido a la caída de presión durante 24 horas. Además, los composites se caracterizaron con difracción de rayos X (XRD) para observar cambios en su estructura cristalina antes y después de las pruebas de adsorción, y análisis termogravimétrico (TGA) para determinar cambios químicos o físicos en el interior del material en contacto con el CO_2 . Los resultados mostraron que la adsorción de CO_2 fue significativa cuando se añadieron óxido de zinc, nanopartículas de óxidos de hierro y nanotubos de carbono a los composites por separado, con valores de 2.37, 3.84 y 4.21 mmol de CO_2 /gramo. En conclusión, estos composites tienen un prometedor poder de adsorción, lo cual muestra un interesante potencial para futuras aplicaciones en reducir las emisiones de CO_2 .

Palabras Clave: Arcilla purificada, NTC, óxido de zinc, ilmenita, magnesioferrita, caolinita, adsorción de CO_2 , composites.

Abstract

Nowadays, carbon dioxide (CO₂) is the highest contributor to the greenhouse effect, responsible for approximately 75% of the total gases released. Then, new materials and technologies have been developed to mitigate the harmful effects of this acid gas. One of these alternatives is CO₂ capture, which uses materials that are constantly being developed. Thus, this study focuses on the composite building of material based on clays from Morona Santiago (COL-307) and Zamora Chinchipe (CZP-303) provinces from Ecuador. These were purified to remove impurities. Then, those were added with different quantities of zinc oxide (ZnO), iron oxide such as ilmenite (FeTiO₃) and magnesioferrite (MgFe₂O₄), and carbon nanotubes (CNTs) to enhance the CO₂ adsorption capacity of clay. These purified clays were composed of kaolinite, which has a porous structure whereby gases could pass through the membrane without any resistance, and the CO₂ had more active sites to separate this gas from others. Therefore, cylindrical and spherical clay pellets were developed with dispersive ZnO, FeTiO₃, MgFe₂O₄ nanoparticles and CNTs. The composites were tested using a high-pressure reactor with pure CO₂ at 25°C. To determine the amount of moles of gas adsorbed by pressure drop for 24 hours. In addition, the composites were characterized with X-ray diffraction (XRD) to observe there were changes in their crystalline structure before and after adsorption tests, and the thermogravimetric analysis (TGA) to observe the chemical or physical changes inside the material in contact with CO₂. The results showed that CO₂ adsorption was significant when zinc oxide, iron oxides nanoparticles, and carbon nanotubes were added to the composites separately, with values of 2.37, 3.84, and 4.21 mmol of CO₂/gram, respectively. In conclusion, these composites have promising adsorption power with exciting potential for future applications to reduce CO₂ emissions.

Key Words: Purified clays, CNTs, zinc oxide, ilmenite, magnesioferrite, kaolinite, CO₂ adsorption, pellets

Table of content

AUTORÍA	i
Acknowledgments	iii
Resumen	iv
Abstract	v
List of Figures	viii
List of Tables	x
Chapter 1	1
1. Introduction	1
1.1. Background	1
1.2. Problem statement	2
1.3. General Objective	2
1.4. Specific Objectives	3
Chapter 2	4
2. Literature Review	4
2.1. CO ₂ pollution	4
2.2. Capture methods of CO ₂	4
2.2.1. Pre-combustion system	5
2.2.2. Post-combustion system	5
2.2.2.1. Absorption solvent methods	5
2.2.2.2. Adsorption–physical separation	6
2.2.2.3. Membrane segregation	6
2.2.2.4. Chemical looping combustion (CLC)	6
2.2.3. Oxy-fuel system	6
2.3. CO ₂ Absorption process	7
2.4. CO ₂ Adsorption process	7
2.5. Clays	8
2.5.1. Clays classification	9
2.5.2. Clays porosity	10
2.6. Metal oxides	11
2.6.1. Iron oxides	11
2.6.2. Zinc oxide	12
2.7. Carbon nanotubes (CNTs)	13
Chapter 3	15
3. Materials and Methodology	15

3.1.	Materials.....	15
3.2.	Methodology.....	15
3.2.1.	Purification of clays.....	15
3.2.1.1.	Preparation of SHMP solution.....	15
3.2.1.2.	Homogenization and clay centrifugation.....	16
3.2.2.	Preparation of metal oxides nanoparticles.....	17
3.2.3.	Molds design and composites building.....	17
3.2.3.1.	Design of clay pellets at different weight percentages.....	18
3.2.4.	Characterization methods.....	19
3.2.4.1.	X-ray Diffraction (XRD).....	20
3.2.4.2.	Thermogravimetric analysis (TGA).....	20
3.2.5.	Porosity Test.....	21
3.2.6.	Reactivity Test.....	22
Chapter 4.....		23
4.	Results and Discussion.....	23
4.1.	Clays Purification.....	23
4.2.	X-ray Diffraction determination of crystalline phases.....	24
4.2.1.	Crystalline phase identification.....	25
4.2.1.1.	Clays.....	25
4.2.1.2.	Metallic oxides.....	29
4.2.2.	Crystalline size.....	32
4.2.2.1.	Iron oxides crystallite size distribution.....	32
4.2.2.2.	Zinc oxide crystallite size distribution.....	35
4.3.	Thermogravimetric analysis (TGA).....	37
4.4.	Porosity test.....	39
4.5.	Reactivity or adsorption test with CO ₂ gas.....	41
Chapter 5.....		44
5.	Conclusion.....	44

List of Figures

Figure 1. Muscovite crystalline structure. a) view of crystal over a plane. b) structure model of the tetrahedral layer of SiO ₄ and AlO ₄ sheets. c) structure model of the octahedral layer.....	8
Figure 2. Crystalline structures of different clays groups and layers. a) kaolinite. b) kerolite. c) allophane. d) phlogopite.....	10
Figure 3. Ilmenite and magnesioferrite crystalline structure.....	12
Figure 4. Wurtzite crystalline structure of zinc oxide.....	13
Figure 5. Carbon nanotubes classification with their different structures.....	14
Figure 6. Purification process of clays COL-307 and CZP-303. a) Homogenization. b) Layer segregation. c)centrifugation of less dense layer.....	16
Figure 7. Retsch milling ball equipment reducing the sample particle size.....	17
Figure 8. Spherical and cylindrical molds with their respective parts.....	18
Figure 9. Spherical and cylindrical pellets of COL-307 after unmolding.....	19
Figure 10. X-ray diffractometry and goniometer with 6 samples.....	20
Figure 11. TGA equipment with a zinc oxide sample after CO ₂ adsorption.....	21
Figure 12. Porosity test of cylindrical pellets during seven days in distilled water.....	21
Figure 13. CO ₂ capture reactor doing the absorption process with the clay sample.....	22
Figure 14. Clay sedimentation and layer separation in 2 L graduated cylinder for 21 days.....	24
Figure 15. X-ray diffraction patterns of pure and raw CZP-303 clay. Crystalline phases are identified by search match method with an a Qualx program and using POW_COD database such as, Quartz, Kaolinite, and Albite.....	26
Figure 16. X-ray diffraction patterns of pure and raw COL-307 clay. Crystalline phases are identified by POW_COD database such as, Quartz, Kaolinite, Albite, and Vermiculite.....	27
Figure 17. X-ray diffraction patterns of reacted and non-reacted iron oxides. Crystalline phases are identified by POW_COD database such as, Ilmenite, and Magnesioferrite.....	30
Figure 18. X-ray diffraction patterns of reacted and non-reacted zinc oxide. Crystalline phases are identified by POW_COD database such as, Zinc oxide, and Zinc carbonate.....	31
Figure 19. Crystalline size of non-reacted Iron oxides prepared at 20Hz frequency.....	33
Figure 20. Crystalline size of reacted Iron oxides prepared at 20Hz frequency.....	34

Figure 21. Crystalline size of non-reacted zinc oxide prepared at 20Hz frequency.	35
Figure 22. Crystalline size of reacted zinc oxide prepared at 20Hz frequency.	36
Figure 23. Crystalline size of recovered zinc oxide prepared at 20Hz frequency.	37
Figure 24. TGA analysis of iron oxides after reacting with CO ₂ and the first derivate.	38
Figure 25. TGA analysis of Zinc oxide after reacting with CO ₂ and the first derivate.	39
Figure 26. Porosity percentage of COL- 307 clay with different compositions of metallic oxides and CNTs.....	41

List of Tables

Table 1. Clays groups classifications with their charge and associated mineral to each group [34].	9
Table 2. Elaboration of clay composites at different percentages of metal oxides nanoparticles and carbon nanotubes.	19
Table 3. Amount of purified clay in relation to the crude sample.....	23
Table 4. Pure and raw CZP-303 clay with the experimental data and POW_COD database of the reflection angle, intensity, and Miller index of identified crystalline phases.....	26
Table 5. Raw COL-307 clay with the experimental data and POW_COD database of the reflection angle, intensity, and Miller index of identified crystalline phases.	28
Table 6. Pure COL-307 clay with the experimental data and POW_COD database of the reflection angle, intensity, and Miller index of identified crystalline phases.	29
Table 7. Reacted and non-reacted iron oxides with the experimental data and POW_COD database of the reflection angle, intensity, and Miller index of identified crystalline phases.	30
Table 8. Non-reacted zinc oxide with the experimental data and POW_COD database of the reflection angle, intensity, and Miller index of identified crystalline phases.	32
Table 9. Reacted zinc oxide with the experimental data and POW_COD database of the reflection angle, intensity, and Miller index of identified crystalline phases.	32
Table 10. Pellets porosity test data with samples immersed in distilled water after 7 days.	40
Table 11. Reactivity test data acquired by spherical pellets after 24 hours.	43

Chapter 1

1. Introduction

1.1. Background

Since the development of industries based on fossil fuels during the last decades has resulted in an increase in CO₂ pollution around the world. Therefore, the main contributor to the greenhouse effect is CO₂, which is responsible for global warming [1]. Gas is usually released mainly by petroleum and gas extraction. This is because these reservoirs store tons of this gas. Governments have created many laws to reduce the amount of CO₂ released into the atmosphere [2]. This has led to the development of technologies to capture this harmful gas. Hence, gas industries have developed ways to entrap CO₂ with the purpose of gas sweetening and eliminating contaminants in the environment.

The sequestration of CO₂ has been developed using its physical and chemical properties to find the most efficient and environment-friendly path to prevent CO₂ from being released into the air [3]. The most widely used adsorption properties allow for the retention of molecules without any reaction of the material. This helps reuse the material several times. This is because there were no internal structural changes. One uses materials that are near gas plants. In this specific case, clays are frequently located in the soil close to the gas reservoir during tropical weather.

Clays are classified as ceramic materials because they are composed of a no metallic atoms and metallic atoms. An interesting characteristic of ceramics is that they are inert materials. This means that they do not easily react with the environment. Ecuadorian clays usually contain large quantities of silicates in their structure [4]. Thus, it is a good candidate for encapsulating CO₂ within its structure because of its many advantages such as porosity, the water retention capacity, malleability among others.

Finally, from the perspective of the methods of encapsulating CO₂ and the adverse effects that the release of indiscriminate quantities of this gas has on the environment. It is inferred that Equatorian clays have the potential to be used as raw materials for CO₂ adsorption using metal nanoparticles and carbon nanotubes to physically attract

molecules towards the porous membrane. The obtained material was characterized using X-ray diffraction (XRD) and thermogravimetric analysis (TGA). Additionally, the porosity was investigated. Finally, the CO₂ adsorption efficiency was evaluated using a chemical reactor that simulates the pressure and temperature conditions found in a gas plant.

1.2. Problem statement

Currently, carbon dioxide is the main greenhouse gas in the world. It is produced by anthropogenic activities, which alter the normal carbon cycle. In general, this is because of the combustion of natural gas, liquefied petroleum gas (LPG), coal, and other carbonaceous sources used in several industrial and domestic activities. Normally, they release large amounts of CO₂ into the atmosphere [5]. Therefore, advanced technologies have sought to selectively remove CO₂ through the design and preparation of adsorbents [6]. However, many of these technologies are expensive because the materials they are made of are nonrenewable. Nevertheless, in Ecuador, there are large quantities of natural resources, such as clays.

They are well known for their absorptive capacities; although low, they can be enhanced for use in CO₂ capture. This can be achieved by generating a composite material by doping or enriching the clays with different metallic oxide (Fe₂O₃, ZnO) nanoparticles and carbon nanotubes (CNTs), which have been shown to be functional in increasing their physical and chemical activities in CO₂ adsorption [7]. Additionally, this work aligns with the goals of the SDGs created by the United Nations in 2015. Thus, this study aims to develop clay pellets with metal oxide nanoparticles as membranes that can separate and capture carbon dioxide originating from combustion exhaust gases.

1.3. General Objective

This research focuses on the design of microporous system structures with the addition of metal oxide nanoparticles and carbon nanotubes. The efficiency of the adsorption and absorption of CO₂ molecules within the membrane was observed by simulating a gas extraction system in reservoirs.

1.4. Specific Objectives

- To study the efficiency of membranes in adsorbing CO₂ molecules inside their structures.
- To analyze the differences between the purified and raw clays according to their morphologies and crystalline structures.
- To evaluate the total porosity and its influence on CO₂ adsorption performance.
- To determine the type of metal oxide or CNTs that can quantitatively improve the adsorption of CO₂ gas.

Chapter 2

2. Literature Review

2.1. CO₂ pollution

Nowadays, industrial development has exponentially increased fuel consumption with the emission of gases that cause the greenhouse effect. The main cause of the greenhouse effect is CO₂, which represents 77% of the total gas released into the atmosphere [8]. This is quantifiable because IPCC reports demonstrate that the worldwide average concentration of CO₂ has reached 400 ppm [9]. This value exceeds the 350 ppm limit for maintaining stable planetary conditions [10]. Thus, the release of this gas has reached critical levels, which can cause imbalances worldwide. This means a progressive increase in Earth's temperature of approximately two °C that affects the entire ecosystem [11]. Considering the negative effects of CO₂ pollution generated mostly by fossil fuels, some solutions are necessary to mitigate this damage. Because it is not realistic to stop all carbon emissions due to the development of civilization, emissions could be reduced with some methods to sequester and capture CO₂ and prevent its release to alleviate the effect of global warming.

2.2. Capture methods of CO₂

As shown in the last chapter, one way to mitigate CO₂ emissions is the sequestration of this gas. Therefore, some industries, such as energy production, refinement plants, and gas reservoirs, which contain many tons of this harmful gas, are coupled with new technologies with different systems to retain CO₂ [12]. These systems are based on fossil fuel combustion, which is pre-combustion, post-combustion, and oxy-fuel systems [13]. All these systems are linked with different methods to segregate CO₂ acidic gas from others and capture them in reservoirs or other chambers. In addition, these methods are based on two physicochemical principles of separation: adsorption and absorption, which are described below with their respective systems.

2.2.1. Pre-combustion system

This procedure typically involves the injection of steam and oxygen to generate a synthesized gas containing hydrogen and carbon monoxide [13]. The synthesized gas is then transformed into carbon dioxide and hydrogen molecules. CO₂ gas is separated into another chamber, and hydrogen is used as the fuel for turbines [14]. In the case of chemical capture, some commercial solvents are used, which lowers the cost of the sequestration technique compared with other solvents. However, they can reduce the efficiency of gas production plants [15]. Another chemical method is the calcium looping process, which uses calcium oxide to capture CO₂ and produce carbonates that are reconverted into oxides when heat increases [16]. There is also an example of physical adsorption. This system uses the Vacuum Pressure Swing Adsorption (VPSA) method, which avoids the release of millions of CO₂ tons into electricity generation plants [17].

2.2.2. Post-combustion system

This dependable system reliably removes CO₂ from flue gases by separating other gases in a purification chamber [12]. Despite the low concentration of CO₂ in flue gas, the driving force of the system is effectively utilized [18]. As the most dependable system in the industry, it is coupled with some sequestration techniques, as outlined in the following description.

2.2.2.1. Absorption solvent methods

This technique involves chemical interaction between the flue gas CO₂ and a solvent, typically composed of amines [16]. This process occurs in two phases. Initially, the CO₂ acid gas interacts with the solvent. The resulting mixture is then heated in a desorber unit, causing the CO₂ to be released and the gas-free solution to return to the absorber chamber [10]. Chemical absorption is the most extensively researched and efficient method; however, it requires significant energy input for heating the desorbed chamber to reclaim the amine solution [16].

2.2.2.2. Adsorption–physical separation

This technique uses a solid surface for CO₂ capture, which involves two distinct mechanisms for physical separation. The first is a physical process that relies on the van der Waals intermolecular forces. Second, chemisorption involves the formation of a covalent bond between the gas and the surface [17]. Materials such as activated carbon, alumina, metallic oxides, and zeolites are commonly employed for physical adsorption due to their porous structure [10].

2.2.2.3. Membrane segregation

The working principle begins to decrease the absorber chamber temperature until the membrane reaches its operational temperature [18]. There are two membrane mechanisms coupled to this method. The first is to pass CO₂ through the permeate membrane from the high-pressure zone to the low-pressure side [19]. Another system employs a microporous solid membrane to effectively isolate CO₂ from a gas stream [20]. These membranes act as selective barriers, allowing only CO₂ to pass through them.

2.2.2.4. Chemical looping combustion (CLC)

CLC process uses two chambers to capture CO₂ and is based on reversible reactions between carbon dioxide and metallic oxides that can form carbonates [21], and these occur in the first reactor where metallic oxides act as CO₂ absorbers that facilitate the formation of carbonates. Then, its carbonate is transported into a second reactor where the sample is calcinated to reconvert carbonate into oxides, and the CO₂ is transformed into gas for storage [19].

2.2.3. Oxy-fuel system

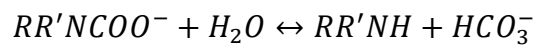
This process refers to the use of an oxygen atmosphere to remove other possible gases present in the usual air atmosphere, where the fuels are combusted to produce water and carbon dioxide as by-products [19]. However, this technique is extremely exothermic.

Therefore, recycled CO₂ is added to decrease the temperature. Then, the water is condensed to purify the CO₂ gas line [22]. The resultant gas is stored or reused to cool the oxy-fuel combustion. This approach is a cost-effective alternative to carbon-capture systems [23].

2.3. CO₂ Absorption process

The CO₂ absorption method is the predominant and theoretically optimal technique for absorbing acidic greenhouse gases and is widely employed on a global scale [24]. These absorptions are divided into two categories: physical and chemical. Thus, physical absorption refers to Henry's law, which states that this process occurs at high pressures and low temperatures [25]. Ionic liquids enhance the physical absorption power due to the recovery of ionic liquids through pressure or temperature variation of high-pressure carbon dioxide [26].

Chemical absorption is the most efficient method compared to all other methods and technologies that have been developed to date [27]. This technique uses a liquid compound that is in contact with gas, which generates a chemical transformation. CO₂ reacts with liquid solvents to form a weakly bonded product, which is recovered by increasing the temperature [25]. This process uses amine solutions, which are the best materials for enhancing the quantity of CO₂ absorbed. Therefore, the following equations show the scheme for the chemical reactions between amines and CO₂ [27].



2.4. CO₂ Adsorption process

The increase in new material design has allowed carbon dioxide adsorption techniques to be applied within the oil and gas industry, potentially lowering the cost of CO₂ sequestration technologies [28]. Typically, this method involves the use of a solid adsorbent material with a large surface area to effectively capture large amounts of gas [29]. The adsorption process relies on several methods, including membrane and chemical looping process [27]. This implies that the discovery and enhancement of compounds for

this purpose is an ongoing process, with new developments constantly emerging with materials such as metal-organic frameworks, nanostructured carbon, metallic oxides, and hybrid organic-inorganic adsorbents [30].

2.5. Clays

Clays are phyllosilicates with a fine-grained structure that results from the decomposition of rock [31]. These minerals have amazing properties, such as plasticity; when a certain amount of water is added, they are converted into moldable materials, which can be rigid when they dry or are fired at high temperatures [32]. The small particle size plays an important role in their physical-chemical properties because it allows for a high diversity of the crystallographic phases present in clays for many applications, especially in the industry [33]. The crystallographic phases of the clays are composed of tetrahedral and octahedral sheets, as seen in [\[Error! No se encuentra el origen de la referencia. a\)](#), where the tetrahedron contains a metallic cation joined by four oxygen atoms shown in [\[Error! No se encuentra el origen de la referencia. b\)](#). A single tetrahedron is joined to each other by oxygen to create a hexagonal mesh pattern. The octahedra are connected to the neighboring octahedra by sharing edges, as seen in [\[Error! No se encuentra el origen de la referencia. c\)](#) [4]. The structure is shown in Figure 1. provided the versatility of these materials for applications in some fields and, for this research, acting as a solid porous material for CO₂ sequestration.

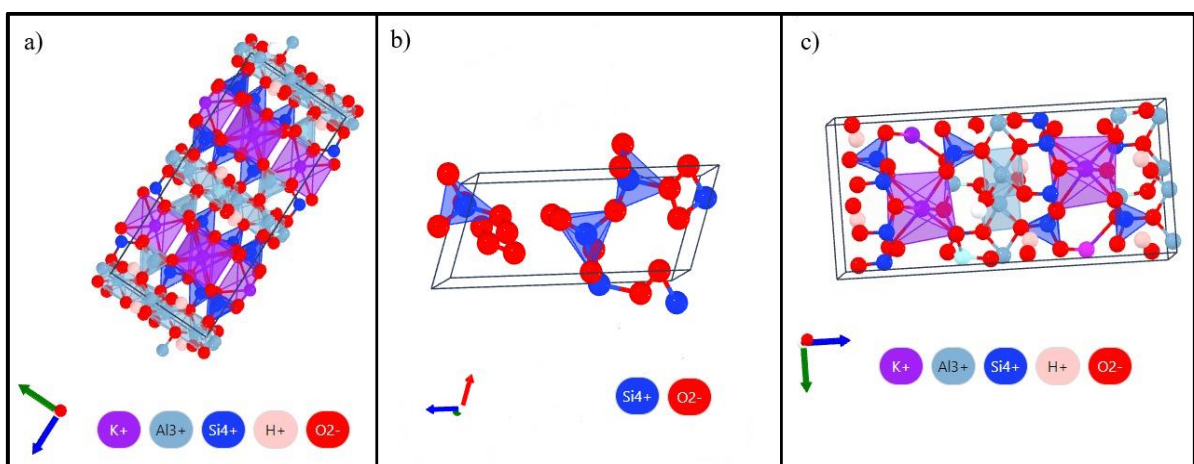


Figure 1. Muscovite crystalline structure. a) view of crystal over a plane. b) structure model of the tetrahedral layer of SiO₄ and AlO₄ sheets. c) structure model of the octahedral layer.

2.5.1. Clays classification

Clays are classified based on their crystallographic structure into several groups depending on the quantity of sheets and the position of their atoms, especially cations, each characterized by specific arrangements of atoms and layers, as described below in **Table 1**.

Table 1. Clays groups classifications with their charge and associated mineral to each group [34].

Clays groups				
N°	Group	Layers	Charge	Associated minerals
1	Kaolin	Diocahedral 1:1 layer	None or water	Kaolinite, dickite , nacrite, halloysite
2	Pyrophyllite, Talc	Diocahedral and trioctahedral 2:1 layer	None	Pyrophyllite, Talc, kerolite
3	Brittle micas	Diocahedral and trioctahedral 2:1 layer	No-water monovalent cations	Illite, muscovite, phlogopite
4	Smectites	Diocahedral and trioctahedral 2:1 layer	Negative layer charge	Hectorite, saponite, Volkonskoite
5	Vermiculite	Diocahedral and trioctahedral 2:1 layer	Negative hydrated cations	Vermiculite
6	Chlorite	Diocahedral and trioctahedral 2:1 layer	Hydrated sheets	Clinochlore, nimite, chamosite
7	Allophane, Imogolite	non-crystalline or poorly crystalline	Positively charged	Imogolite, Allophane

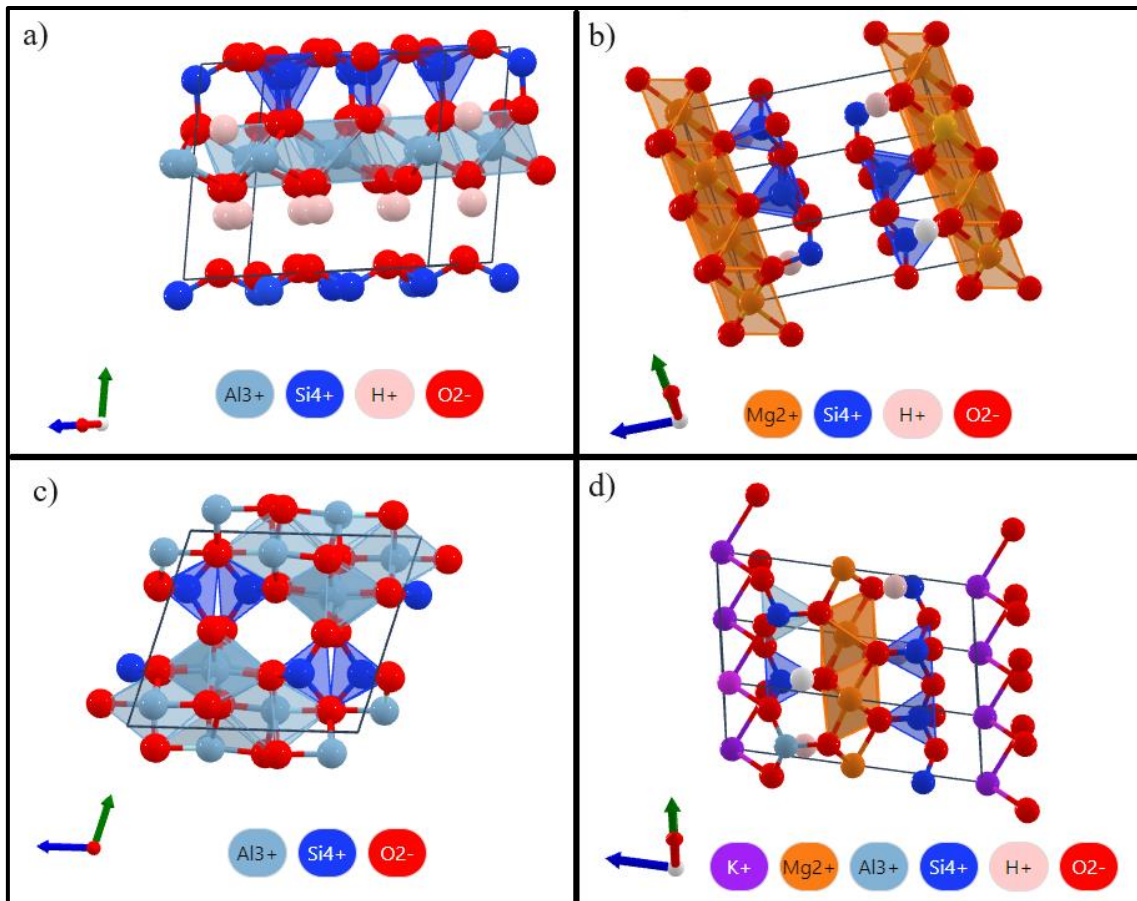


Figure 2. Crystalline structures of different clays groups and layers. a) kaolinite. b) kerolite. c) allophane. d) phlogopite.

2.5.2. Clays porosity

The swelling of clays is related to the specific surface area and crystallographic structure of all types of clays, as it seems before these structures have an arrangement of 1:1 and 2:1 layer [35]. These configurations have exceptional physicochemical properties that improve their applications in the development of capture systems [33]. This is because clay porosity in a simple look appears compact. Therefore, its porosity depends on the arrangement of atoms due to the space between the octahedral layers.

Additionally, the size of the pores is influenced by the nature of the cations present in the octahedral sheets. It means that small cations allow closer packing of the layers, which reduces the interlayer space between the sheets and decreases the porosity of the material both qualitatively and quantitatively [35]. Meanwhile, large cations can lead to greater

separation between layers because of the large size of these metallic ions, which increases the porosity of the clay [36].

2.6. Metal oxides

2.6.1. Iron oxides

Iron oxides are formed from Fe-containing rocks that undergo natural weathering processes both on land and in oceans [37]. These iron oxides have been found in many crystalline structures. The ilmenite (FeTiO_3) compound has a structure with two cations, Fe and Ti, coordinated in an octahedral arrangement, with oxygen having three octahedral edges shared among the cation octahedra of the same kind. This structure is named sesquioxide, and it is derived from a hexagonal, close-packed structure [38]. This solid has magnetic properties due to the presence of metallic ions, such as iron. This same is observed for magnesioferrite (MgFe_2O_4), another iron oxide coupled with a Mg cation. The crystalline structure is a face-centered cubic structure and is characterized by their two-site atomic arrangement of cations: tetrahedral oxygen coordination and octahedral oxygen coordination [39]. Both crystalline phases are present in the powder iron oxide used in this study. Thus, there are some structures containing iron oxides of a nanometer size that enhance their physicochemical properties [40]. This study focuses on two morphologies containing iron oxides, which are ilmenite and magnesioferrite.

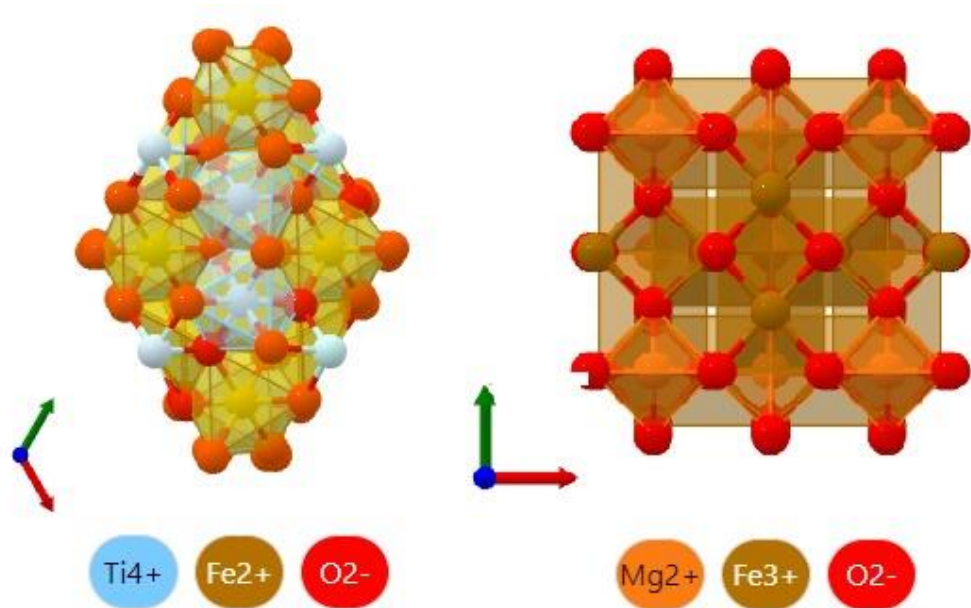


Figure 3. Ilmenite and magnesioferrite crystalline structure.

2.6.2. Zinc oxide

Zinc oxide ore is a product of the oxidation of metallic zinc [41]. Nowadays, ZnO is produced in three ways for commercialization and has a wide range of applications, such as, photocatalytic degradation of organic dyes in aqueous solutions [42], activator of organic accelerators in the vulcanization process of rubber [43], among others. These applications have led to the development of some nanostructures, like nanowires and nanobelts, among others, depending on the synthesis methodology and growth conditions [44]. The crystal of ZnO is a wurtzite, which has a hexagonal shape and is composed of a set of alternating planes of O^{2-} and Zn^{2+} ions that are connected in a tetrahedral manner as shown in **Figure 4** [45]. The most interesting properties include good thermal conductivity, tunable electrical properties, piezoelectricity, and gas sensing [44]. This property allows the entrapment of CO_2 and other acidic gases and enhances the existing technologies coupling ZnO in the capture system, which is the focus of this research.

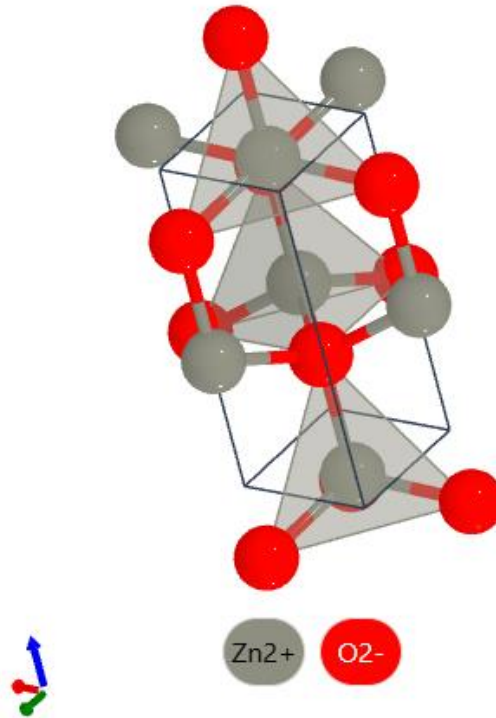


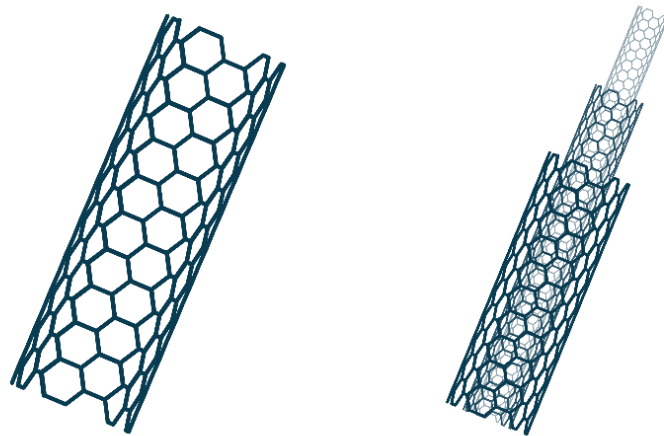
Figure 4. Wurtzite crystalline structure of zinc oxide.

2.7. Carbon nanotubes (CNTs)

Carbon nanotubes have been discovered only four decades ago. These structures belong to the family of fullerenes [46]. This carbon structure has sp^2 hybridization, which allows for the molding of the structure in a cylindrical way, where each carbon is joined by two other carbons, forming sheets in a hexagonal lattice [47]. The shape and size of cylindrical graphene nanotubes provide exceptional properties, including electrical, thermal, and mechanical strength [48]. Its properties can change depending on the quantity of nanotube sheets. These structures are classified into single-, double-, and multi-walled carbon nanotubes [46], as shown in Figure 5. Therefore, some studies show awesome potential applications, such as the development of new technological devices such as semiconductors [49] or the enhancement of the characteristics of existing materials that are doped with these CNTs.

CNTs are good candidates for removing inorganic and organic phases. This specific case focuses on CO_2 removal from the gas lines. It is possible due to the larger areas of the CNT structure and porosity of the material [50]. Adsorption occurs via two mechanisms.

The first is chemisorption, in which chemical interactions occur between the molecules of the substance being adsorbed and functional groups on the surface of the adsorbent material [51]. Second, the physisorption process occurs owing to the van der Waals interactions between the CNTs and the adsorbate [52]. The adsorption mechanism of CNTs is physisorption because their chemical composition remains unchangeable and the desorption of the adsorbents at relatively low temperatures [52]. Thus, the development and research of this new material promises to improve the CO₂ adsorption efficiency of existing systems, as many researchers have shown the high adsorptive strength of CNTs, especially in multi-wall structures, due to their porosity and size [51].



a) Single-walled CNT

b) Multi-walled CNTs

Figure 5. Carbon nanotubes classification with their different structures.

Chapter 3

3. Materials and Methodology

3.1. Materials

Clays were obtained from the soil in eastern Ecuador. Specifically, we used two clays from different locations: COL-307 clay from the North of Limon Indanza canton, Morona-Santiago province located at longitude and latitude $78^{\circ} 25' 18.70''$ W $2^{\circ} 57' 03.49''$ South respectively, and CZP-303 clay from 0.2 Km SW of Panguintza, course, North of the La Saquea, Zamora province located at longitude and latitude $78^{\circ} 49' 09.16''$ W $3^{\circ} 54' 18.08''$ S, respectively. Metal oxides, such as iron oxides, were obtained from the purification process of sand SYA-104 located in Anconcito beach in the province of Santa Elena, and iron oxide was obtained from the Laboratory of Chemistry of Yachay Tech University. Finally, the carbon nanotubes were supplied by Professor Luis Corredor from Yachay Tech University.

3.2. Methodology

This section describes the main steps in the development and design of clay membranes with metal oxide nanoparticles and CNTs. The main steps were the purification of clays, preparation of metal oxide nanoparticles, design of clay pellets with different percentages of metal oxides and carbon nanotubes, and methods of characterization with sample preparation, reactivity, and porosity tests.

3.2.1. Purification of clays

Clay purification has two main stages: the preparation of sodium hexametaphosphate to separate the layers in the clay solution, and the segregation of layers in a cylinder, which is obtained by centrifugation.

3.2.1.1. Preparation of SHMP solution.

SHMP solution (Sodium Hexametaphosphate) was prepared at a concentration of 1 M in a volume of 250 ml. First, the 152.94 g of SHMP in powder was introduced into the beaker, and distilled water was added until it reached a mark of 200 ml. Then, stirring the

resulting solution was stirred for 4 h. Finally, the solution was placed in a round-bottomed flask and rooted to the volumetric mark.

3.2.1.2. Homogenization and clay centrifugation

First, 400 g of clay was added and the mixture was placed in a 2 L beaker. Then, 23.5 mL of sodium hexametaphosphate (1 M) was added. Next, 1600 mL distilled water was added. A homogenizer was placed inside the beaker, which was the MTOPS model SR30, where the homogenization conditions were to take the solution at a speed of 12700 rpm for 30 min for the SHMP solution and distilled water with clay to mix completely. The mixture was then left in a 2 L graduated cylinder for approximately 21 days. After those days, separation in layers of clay was observed, which was removed using a syringe and a hose. The first layer is an organic phase, the second and third layers are the purified clay of interest, and the last layer is the heaviest. The second and third phases were removed. These phases proceeded using a centrifuge with a rotor N° 4 of 50 ml Falcon tubes to separate the liquid phase from the solid phase. For this, we used the conditions of 10.500 rpm for 30 min. Finally, it separates the solid phase from the liquid phase, which is discarded and left to dry in a tray for three days or until the purified clay is completely dry. This procedure was repeated many times until sufficient purified material was obtained, as shown in **Figure 6**.



Figure 6. Purification process of clays COL-307 and CZP-303. a) Homogenization. b) Layer segregation. c) centrifugation of less dense layer.

3.2.2. Preparation of metal oxides nanoparticles

The metallic oxides of iron oxides and zinc oxide were ball-milled to reduce their particle size to the nanometer level. This equipment was a RETSCH model MM500 NANO RETSCH of high energy with a maximum frequency of 35 Hz. Inside the baskets, the oxides were placed with steel balls and prepared under the following conditions: different frequencies of 20 and 35 Hz were applied for 30 min. This yielded different particle sizes for each oxide sample.



Figure 7. Retsch milling ball equipment reducing the sample particle size.

3.2.3. Molds design and composites building

For this study, two types of molds were developed: cylindrical and spherical. These molds are designed with surgical steel to avoid chemical interaction between the material and mold, which causes some errors in the measurement of their properties. The cylinder was composed of four parts: a cylinder, two lids, and a remover. The spherical molds were composed of two half-spheres.

These molds had the following sizes and diameters to ensure the replication of molding with clays under these conditions. The cylindrical mold had a height of 20 mm and a

diameter of 10 mm. In addition, it is designed as a piece that allows the removal of cylinders without the material suffering any change in shape. The spherical shape has a diameter of 10 mm.



Figure 8. Spherical and cylindrical molds with their respective parts.

3.2.3.1. Design of clay pellets at different weight percentages

Clay pellets were prepared using different quantities of metal oxide nanoparticles and carbon nanotubes in a systematic process. First, the solid clays were pulverized until they were converted into a powder. It weighed 13 g of clay to prepare four cylindrical pellets and six spheres. It was hydrated with 6 ml of distilled water to obtain dough consistent enough to mold them and create these two types of pellets. Therefore, this procedure was repeated using zinc oxide and iron oxide nanoparticles retrieved from a frequency of 20 Hz, with a mass concentration of 1% and carbon nanotubes of 0.01% in mass. In addition, it is necessary to create a mixture of metallic oxide nanoparticles with CNTs by weight with respect to clay, as shown in **Table 2**. Elaboration of clay composites at different percentages of metal oxides nanoparticles and carbon nanotubes.

Table 2. Elaboration of clay composites at different percentages of metal oxides nanoparticles and carbon nanotubes.

Preparation of pellets samples						
N°	Clay	Zinc Oxide (%w)	Iron oxides (%w)	CNTs (%w)	N° Spheres	N° Cylinders
1	COL-307	0.00	0.00	0.00	9	4
2	COL-307	1.00	0.00	0.00	6	4
3	COL-307	0.00	1.00	0.00	6	4
4	COL-307	0.00	0.00	0.01	6	4
5	COL-307	1.00	1.00	0.00	6	4
6	COL-307	1.00	0.00	0.01	6	4
7	COL-307	0.00	1.00	0.01	6	4
8	COL-307	0.50	0.50	0.01	6	4



Figure 9. Spherical and cylindrical pellets of COL-307 after unmolding.

3.2.4. Characterization methods

These methods were used to determine the crystalline phases present in the raw and purified materials to determine their crystalline structure, particle size with X-ray Diffraction (XRD), and weight loss by thermogravimetric analysis (TGA). All these methods were implemented before and after the reactivity test of CO₂ absorption to observe the changes in the final material.

3.2.4.1. X-ray Diffraction (XRD)

X-ray Diffraction was performed with a sampling of clays and metallic oxides to determine the crystalline phases in each material using an X-ray diffractometer for polycrystalline samples, D/teX Ultra detector, and SmartLab Studio II software. In addition, an X-ray generator operated at 40 kV and 15 mA, CuK(alpha) radiation source (sealed tube), 2θ scanning axis, 0.01° pitch width, $5-100^\circ$ scanning range, $10^\circ/\text{min}$ speed, and D/tex Ultra2 detector in 1D scanning mode were used for data acquisition. Then, the analysis of phase identification for these samples was performed using the QUALX program [53], and the POW_CODINO as database [54].



Figure 10. X-ray diffractometry and goniometer with 6 samples.

3.2.4.2. Thermogravimetric analysis (TGA)

This analysis was performed only on metal oxide nanoparticles to demonstrate whether these metals reacted with CO_2 to form carbonates or produced any chemical reaction. Therefore, it is necessary to use both inert and oxidizing atmospheres for this technique with a speed increase of $20^\circ/\text{min}$, starting at 20°C and continuing until 900°C in a $100\ \mu\text{L}$ platinum crucible. This analysis was performed using TGA equipment, a Thermogravimetric Analyzer from TA Instruments, and model TGA 55, as shown in **Figure 11**.



Figure 11. TGA equipment with a zinc oxide sample after CO₂ adsorption.

3.2.5. Porosity Test

The porosity test was performed using the solvent method, which consisted of adding 55 ml of distilled water. Then, inside the beakers, one cylindrical dry pellet of each of the eight samples was placed in a different composition. These pellets were weighed to determine the difference in weight with wet pellets after seven days of leaving the beaker with distilled water solvent, as shown in **Figure 12**, to determine the quantity of water absorbed. This difference and relative porosity were determined using the following equation:

$$\text{Relative Porosity (\%)} = \frac{\text{Wet Volume} - \text{Dry Volume}}{\text{Wet volume}} \times 100$$

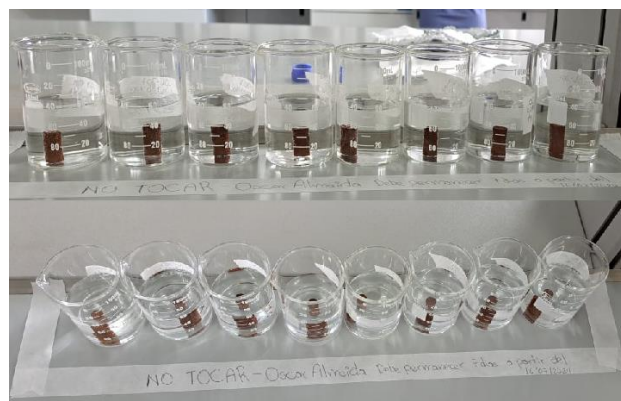


Figure 12. Porosity test of cylindrical pellets during seven days in distilled water.

3.2.6. Reactivity Test

The clay pellets were weighed three times to calculate the average weight. Subsequently, the specimens were inserted into the reactor chamber, which was meticulously attached to the CO₂ gas line to prevent potential leakage. Additionally, sensors were connected to monitor the temperature and pressure during the commencement of the capture test. The test was performed using a reactor Parr 4838 controller. The initial temperature was 25°C, and the gas line was opened until the chamber reached 500 *psig*. The reactor gathers data for at least 24 h until there is no further decrease in pressure. After the test, the collected data was saved, and the gas extraction machine was turned on. The gas pressure in the reactor was gently released to avoid any explosion or abrupt outgassing until it reached 0 *psig*. Finally, the reactor was disassembled to recover the sample from the pellets and was reweighed to observe any changes in the composition of the material.



Figure 13. CO₂ capture reactor doing the absorption process with the clay sample.

Chapter 4

4. Results and Discussion

4.1. Clays Purification

The purification method consisted of sedimentation and layer separation based on the density of the material in the solution. The percentage yield of our separation process was relatively low, which for the COL-307 clay was 21.6%, while the CZP-303 clay, it was even lower, with a percentage of clay recovered of 12.5%, as shown in **Table 3** Despite the low yield of the purified phase, a large amount of the heavy phase, which contains much quartz and other heavy minerals denser than pure clays, was discarded in both clays, especially in the COL-307. This occurs because the solution of SHMP was properly homogenized with the whole mixture in both clays and water, which allowed the separation of the compounds present therein, such as the organic phase, which was the least dense of all solutions. The precipitated layer exhibited two phases, as shown in

Figure 14. The first phase is lighter, with a small particle size, and contains the purified sample of interest., and the other phase is the heaviest, composed mainly of quartz (silicon oxide). It is demonstrated by analyzing each phase of clay using an X-ray diffraction technique, as described in section **X-ray Diffraction (XRD)**3.2.4.1. The developed method of purification uses less reactive material and time to effectively separate the purified phase from the other contaminants present in clay soil. Hence, other works mention a more complex procedure to reach a purified clay [55]. It represents a higher cost-benefit ratio than our purification system.

Table 3. Amount of purified clay in relation to the crude sample.

Clay purification data				
Clay Code	Raw Clays	Sedimentation time	Purified Amount	Yield
CZP-303	1200 g	21 days	150 g	12.5%
COL-307	1200 g	21 days	260 g	21.6%



Figure 14. Clay sedimentation and layer separation in 2 L graduated cylinder for 21 days.

4.2. X-ray Diffraction determination of crystalline phases

The materials used in this study, such as clays, metal oxides, and carbon nanotubes, were analyzed and characterized using X-ray diffraction to determine the composition and crystalline phases present in each sample. Therefore, the diffraction patterns of the compounds were obtained before and after their treatments, either purification in the case of clays or in the case of metal oxides before and after the reactivity test with CO₂. This was done to determine whether there were changes in their compositions after the treatment of each sample.

4.2.1. Crystalline phase identification

4.2.1.1. Clays

The CZP-303 clay was characterized using an X-ray diffractometer. The diffraction patterns of both the raw clay and purified clay forms were obtained, as shown in **Figure 15**. Using the methodology described in the section **3.2.4.1**, the following phases were observed: quartz, albite, and kaolinite. In this case, kaolinite corresponds to the kaolin group in the classification of clay. Quartz is silicate and albite is feldspar. Then, some characteristic peaks in the range from 10 to 30 of 2θ degrees were observable. The peaks in the 2θ of 12.36° , 22° and 26.69° correspond to the following crystallographic planes: kaolinite (0 0 2), albite (2 0 -1) and quartz (1 0 -1). In addition, there are other peaks that help us to ensure that the crystallographic phases are present, as described in **Table 4** with their h reflection angles, Miller (miller index), intensity, and phases.

As see in **Figure 15** shows the peak identification of raw and pure clay, it still contained large amounts of quartz-(silicon oxide) as the raw sample because these are large particles that are usually present only in the heavy phase and still appear in the purified phase. Therefore, the same characteristic quartz peaks are observed at angles of 20.86° and 50.15° in both patterns, with only slightly different intensities. This means that the purification was not entirely effective. This can be achieved because some of the clay settled in beakers, which have a wider diameter in relation to the cylinders, and density separation in graduated cylinder by gravity did not occur correctly. However, the semi-quantitative analysis in QualX [53] indicated that a certain percentage of quartz disappeared after treatment, and the kaolinite phase increased; however, it was not sufficient to avoid the presence of silicon oxide compounds in the sample. In addition, albite was not eliminated after purification owing to the presence of peaks at 2θ angles of 22° and 27.76° with the miller index of (2 0 -1) and (2 0 -2) with small intensities, in the CZP-303 pure sample.

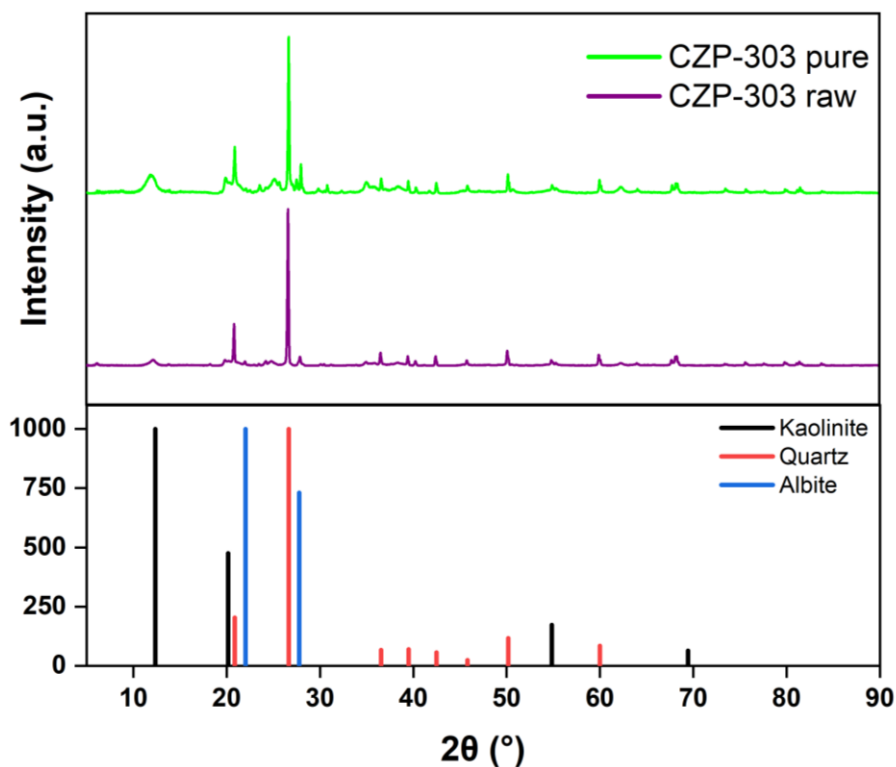


Figure 15. X-ray diffraction patterns of pure and raw CZP-303 clay. Crystalline phases are identified by search match method with an a Qualx program and using POW_COD database such as, Quartz, Kaolinite, and Albite.

Table 4. Pure and raw CZP-303 clay with the experimental data and POW_COD database of the reflection angle, intensity, and Miller index of identified crystalline phases

Reflection angle 2θ						
Raw Clay	Pure Clay	POW_COD database				
2θ(°)	2θ(°)	2θ(°)	(hkl)	Intensity	Compound	Formula
12.243	12.31	12.3646	(0 0 2)	1000	Kaolinite	Al ₂ Si ₂ O ₅ (OH) ₄
20.273	20.38	20.1393	(1 1 0)	475.74	Kaolinite	Al ₂ Si ₂ O ₅ (OH) ₄
20.843	20.92	20.8629	(1 0 0)	203.68	Quartz	SiO ₂
22.023	21.37	22.0089	(2 0 -1)	1000	Albite	NaAlSi ₃ O ₈
26.623	26.69	26.6455	(1 0 -1)	1000	Quartz	SiO ₂
27.893	28.01	27.7625	(2 0 -2)	731.86	Albite	NaAlSi ₃ O ₈
36.533	36.59	36.5534	(2 -1 0)	67.47	Quartz	SiO ₂
39.543	39.51	39.4765	(1 0 -2)	70.78	Quartz	SiO ₂
42.443	42.52	42.4617	(2 0 0)	57.89	Quartz	SiO ₂
45.783	45.84	45.8055	(2 0 -1)	25.42	Quartz	SiO ₂
50.113	50.19	50.1511	(2 -1 2)	118.28	Quartz	SiO ₂
54.833	54.92	54.8318	(1 3 6)	173.16	Kaolinite	Al ₂ Si ₂ O ₅ (OH) ₄
59.923	60.00	59.9725	(3 -1 -1)	86.04	Quartz	SiO ₂
68.463	68.17	69.4398	(2 0 8)	64.52	Kaolinite	Al ₂ Si ₂ O ₅ (OH) ₄

On the other hand, the COL-307 X-ray patterns were acquired before and after purification. As shown in **Figure 16**, this experimental pattern was compared with the POW_COD database using QualX [54] to determine the crystalline phases, which are vermiculite, quartz, albite, and kaolinite. Additionally, these crystalline phases also appear in CZP-303, except for vermiculite. For this there is a characteristic peak normally observed in the reflection plane (0 6 0) in the XRD according to the bibliography [56]. However, vermiculite was identified in the crystallographic plane (0 0 4) with an experimental reflection angle of 12.18° in the pattern of raw clay. Besides, in a pure clay pattern, the most distinctive peak appears at 18.31° with a Miller index of (0 0 6) with a high intensity. All distinctive peaks of each of these four phases were classified in the **Table 5** for raw and **Table 6** pure clay with their respective experimental and reported crystallographic data on POW_COD database [54].

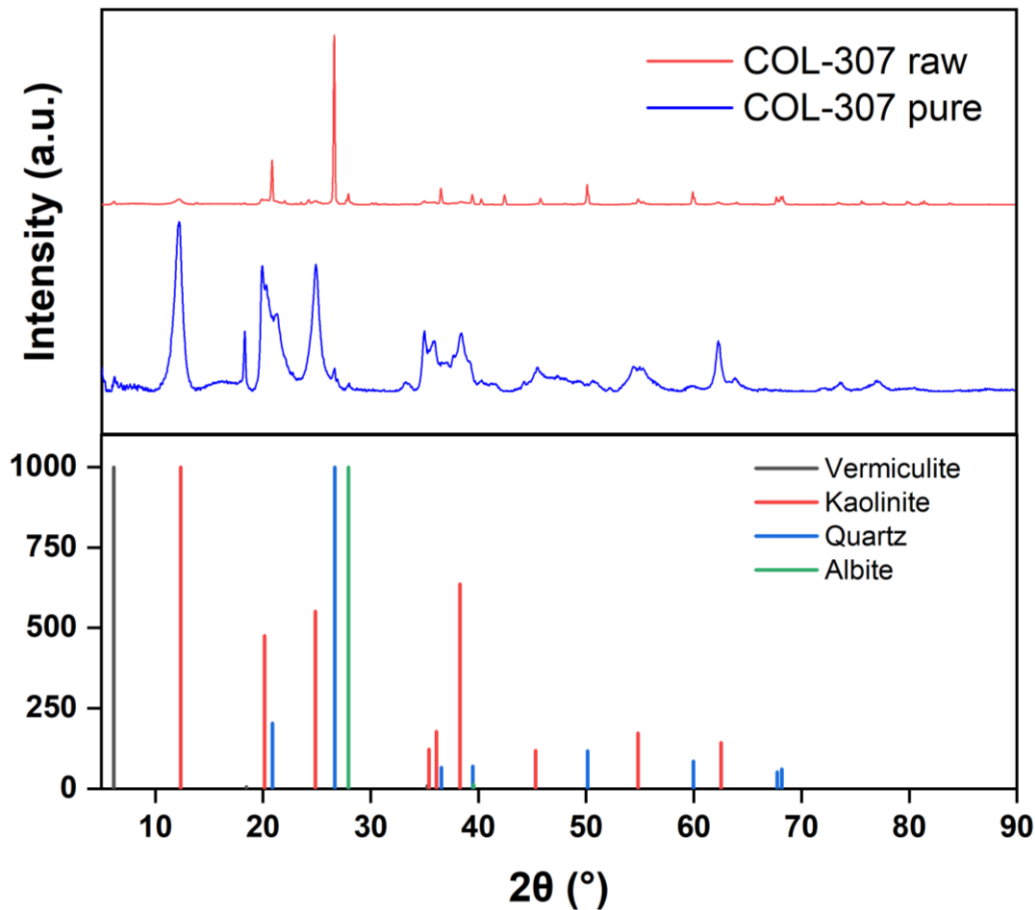


Figure 16. X-ray diffraction patterns of pure and raw COL-307 clay. Crystalline phases are identified by POW_COD database such as, Quartz, Kaolinite, Albite, and Vermiculite.

In **Table 5**, COL-307 raw clay shows three crystallographic phases, which are quartz, albite, and vermiculite. Quartz was the most observable phase in this diffraction pattern, and eight peaks were identified in the experimental data. As with the raw CZP-303 clay, the characteristic peak at a $2\theta = 26.62^\circ$ corresponds to quartz and its plane of reflection (1 0 -1). Hence, raw COL-307 contains a high amount of this phase. Nevertheless, this peak disappeared completely of the COL-307 clay by purification process as it seemed in **Figure 16**. Therefore, this allowed the appearance of other purified phases of this clay, which were obscured or overlapped by the presence of quartz. The other crystallographic phases of pure COL-307 have been described in detail in **Table 6**. The acquired data showed the presence of a majority crystalline phase, kaolinite. Its crystallographic phase has the three most intense and observable peaks at 12.19° , 19.94° , and 24.9° 2θ with the planes (0 0 2), (1 1 0), and (0 0 4) as seen in the diffraction pattern of the blue label.

Table 5. Raw COL-307 clay with the experimental data and POW_COD database of the reflection angle, intensity, and Miller index of identified crystalline phases.

Reflection angle 2θ						
Raw Clay		POW_COD database				
2θ	Intensity	2θ	(hkl)	Intensity	Compound	Formula
12.184	33.044	12.2814	(0 0 4)	13.39	Vermiculite	$Mg_3Si_4O_{10}(OH)_2$
20.854	262.491	20.8629	(1 0 0)	203.68	Quartz	SiO_2
26.624	1000	26.645	(1 0 -1)	1000	Quartz	SiO_2
27.934	66.973	27.9141	(0 0 2)	1000	Albite	$NaAlSi_3O_8$
36.534	97.042	36.5534	(0 0 4)	67.47	Quartz	SiO_2
39.454	60.81	39.4765	(1 0 -2)	70.78	Quartz	SiO_2
		39.5397	(1 -1 -3)	14.97	Albite	$NaAlSi_3O_8$
50.124	119.126	50.1511	(2 -1 2)	118.28	Quartz	SiO_2
59.934	76.748	59.9725	(3 -1 -1)	86.04	Quartz	SiO_2
67.714	45.602	67.758	(3 -1 -2)	53.47	Quartz	SiO_2
68.294	49.464	68.1623	(2 0 -3)	62.38	Quartz	SiO_2

Table 6. Pure COL-307 clay with the experimental data and POW_COD database of the reflection angle, intensity, and Miller index of identified crystalline phases.

Reflection angle 2θ of COL-307 pure clay						
Pure Clay		POW COD database				
2θ	Intensity	2θ	(hkl)	Intensity	Compound	Formula
6.226	87.693	6.1319	(0 0 2)	1000	Vermiculite	Mg ₃ Si ₄ O ₁₀ (OH) ₂
12.196	1000	12.3646	(0 0 2)	1000	Kaolinite	Al ₂ Si ₂ O ₅ (OH) ₄
18.306	355.496	18.4666	(0 0 6)	6.36	Vermiculite	Mg ₃ Si ₄ O ₁₀ (OH) ₂
19.936	741.177	20.1393	(1 1 0)	475.74	Kaolinite	Al ₂ Si ₂ O ₅ (OH) ₄
24.906	750.28	24.8762	(0 0 4)	551.94	Kaolinite	Al ₂ Si ₂ O ₅ (OH) ₄
35.006	357.624	35.4035	(2 0 -2)	123.48	Kaolinite	Al ₂ Si ₂ O ₅ (OH) ₄
		35.2626	(2 0 -4)	10.39	Vermiculite	Mg ₃ Si ₄ O ₁₀ (OH) ₂
35.926	298.092	36.1045	(1 3 1)	179.2	Kaolinite	Al ₂ Si ₂ O ₅ (OH) ₄
38.436	344.936	38.3019	(1 3 2)	636.62	Kaolinite	Al ₂ Si ₂ O ₅ (OH) ₄
45.526	143.306	45.2857	(1 3 4)	120.24	Kaolinite	Al ₂ Si ₂ O ₅ (OH) ₄
54.426	149.346	54.8318	(1 3 6)	173.16	Kaolinite	Al ₂ Si ₂ O ₅ (OH) ₄
62.306	298.395	62.5286	(3 3 -1)	143.91	Kaolinite	Al ₂ Si ₂ O ₅ (OH) ₄

4.2.1.2. Metallic oxides

Diffraction patterns of the reacted and non-reacted iron oxides were acquired, as shown in **Figure 17**. There was no change in the representative peaks of these two patterns. This is demonstrated using the cards retrieved by the POW_COD database [54] obtained after the XRD analysis, where the most intense peaks at 32.88° and 35.44° of 2θ appear in both curves, in the reflection planes (1 0 4), and (3 1 1) which correspond to the ilmenite and magnesioferrite phases. This means that after exposing the iron oxides to CO₂ gas, the material does not undergo any chemical reaction and remains unalterable in its composition. Besides, other characteristic peaks of each phase appear in the crystallographic analysis in detail, as shown in **Table 7**. Therefore, iron oxides do not require any specific treatment to recover the material after CO₂ sequestration.

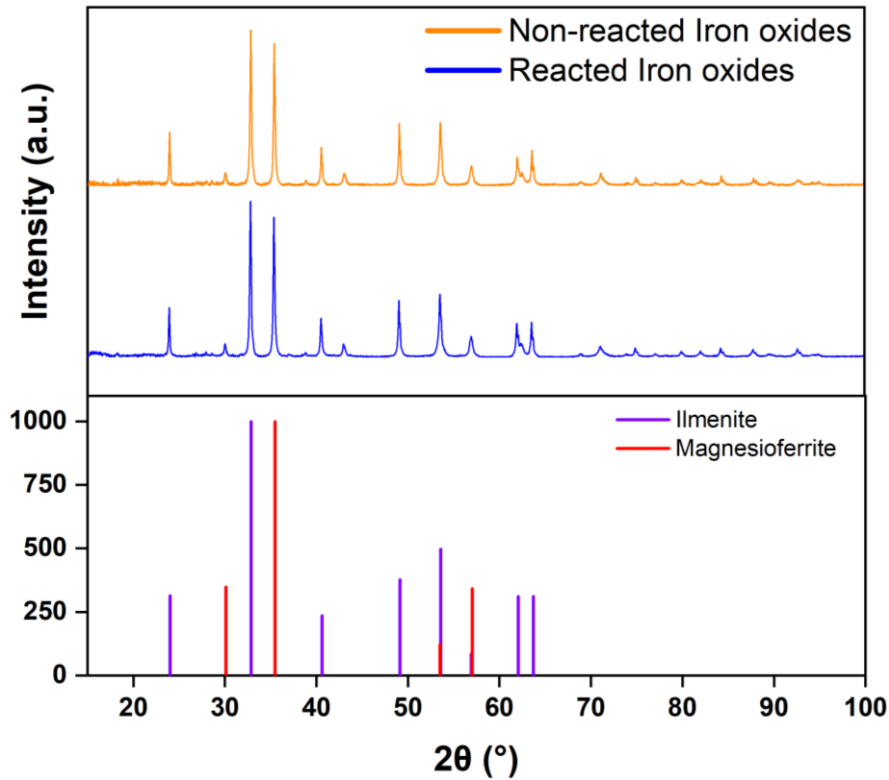


Figure 17. X-ray diffraction patterns of reacted and non-reacted iron oxides. Crystalline phases are identified by POW_COD database such as, Ilmenite, and Magnesioferrite.

Table 7. Reacted and non-reacted iron oxides with the experimental data and POW_COD database of the reflection angle, intensity, and Miller index of identified crystalline phases.

Reflection angle 2θ of Iron oxides						
Iron oxide	Reacted Iron oxide	POW_COD database				
		2θ	(hkl)	Intensity	Compound	Formula
23.997	23.964	23.995	(1 0 -2)	314.62	Ilmenite	FeTiO ₃
30.067	30.059	30.1153	(2 2 0)	348.49	Magnesioferrite	MgFe ₂ O ₄
32.887	32.849	32.8593	(1 0 4)	1000	Ilmenite	FeTiO ₃
35.447	35.414	35.4802	(2 -1 0)	703.9	Ilmenite	FeTiO ₃
		35.4715	(3 1 1)	1000	Magnesioferrite	MgFe ₂ O ₄
40.607	40.559	40.6122	(2 -1 -3)	235.32	Ilmenite	FeTiO ₃
49.132	49.084	49.1316	(2 0 -4)	378.21	Ilmenite	FeTiO ₃
53.617	53.574	53.5899	(2 -1 -6)	497.41	Ilmenite	FeTiO ₃
		53.4851	(4 2 2)	122.3	Magnesioferrite	MgFe ₂ O ₄
56.997	56.989	56.9271	(1 0 -8)	84.55	Ilmenite	FeTiO ₃
		57.0156	(5 1 1)	341.67	Magnesioferrite	MgFe ₂ O ₄
62.032	62.149	62.0543	(3 -2 -4)	311.17	Ilmenite	FeTiO ₃
63.652	63.599	63.7049	(3 0 0)	311.49	Ilmenite	FeTiO ₃

Unlike iron oxides, zinc oxide exhibited a distinct XRD pattern. The diffraction patterns were obtained before and after CO₂ gas exposure, as illustrated in **Figure 18**. The patterns of both reacted and unreacted zinc oxides appear nearly identical. However, closer examination reveals subtle low-intensity peaks that are barely noticeable in the curve representing the reacted sample. These new peaks indicate the appearance of another crystalline phase, which was identified as zinc carbonate crystallites. Two distinctive peaks confirm the presence of carbonates, which are in the reflection planes (1 0 -2) and (1 0 4) with small experimental intensities at 38.9 and 80.27 located at 24.97° and 32.44° of 2θ angles, respectively. The appearance of this new crystalline phase indicates that the composition of the material changed after the CO₂ capture test. From the crystalline phase identification, this new phase was confirmed in the reacted zinc oxide pattern comparing the reported cards using the POW_COD database [54] where peaks were shown at 25.06° and 32.56° with the same reflection planes. The other peaks were labeled and listed with their respective crystalline phases using the Miller index of Bragg reflection planes in the following **Table 8** and **9**.

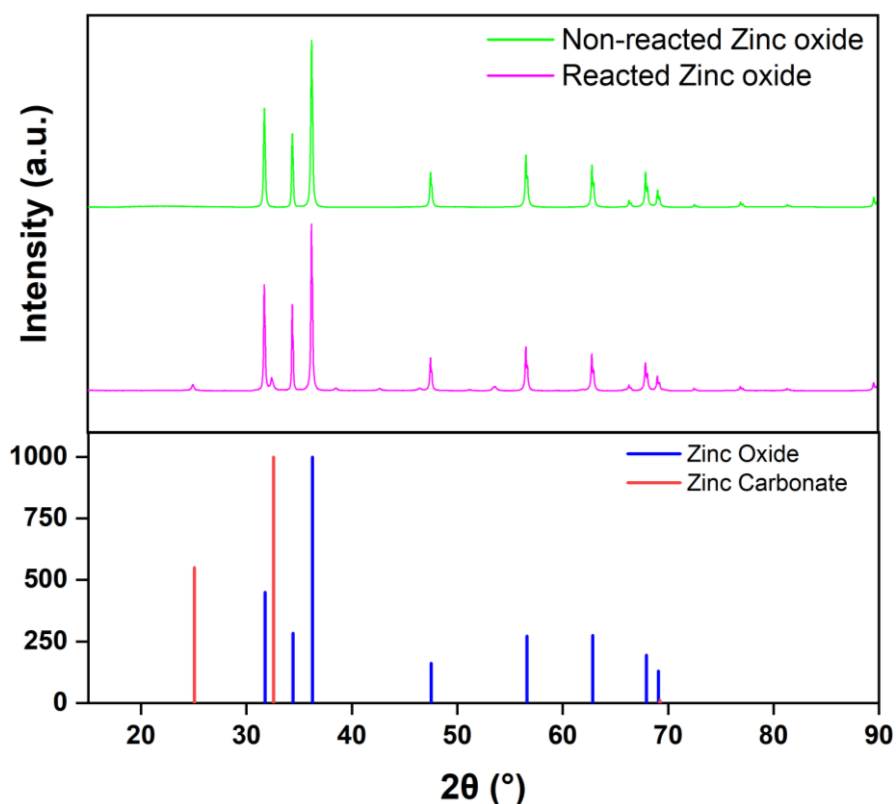


Figure 18. X-ray diffraction patterns of reacted and non-reacted zinc oxide. Crystalline phases are identified by POW_COD database such as, Zinc oxide, and Zinc carbonate.

Table 8. Non-reacted zinc oxide with the experimental data and POW_COD database of the reflection angle, intensity, and Miller index of identified crystalline phases.

Reflection angle 2θ of non-reacted Zinc oxide					
Zinc oxide		POW COD database			
2θ	Intensity	2θ	(hkl)	Intensity	Compound
31.771	592.843	31.7717	(1 0 0)	449.99	ZnO
34.421	441.737	34.42	(0 0 2)	283.79	ZnO
36.256	1000	36.2554	(1 0 1)	1000	ZnO
47.546	208.796	47.5387	(1 0 2)	162.51	ZnO
56.601	313.03	56.5985	(2 -1 0)	272.13	ZnO
62.861	252.455	62.8538	(1 0 3)	275.02	ZnO
67.951	211.922	35.2626	(2 -1 2)	194.61	ZnO
69.091	104.172	38.3019	(2 0 1)	129.79	ZnO

Table 9. Reacted zinc oxide with the experimental data and POW_COD database of the reflection angle, intensity, and Miller index of identified crystalline phases.

Reflection angle 2θ of reacted Zinc oxide					
Zinc oxide sample		POW COD database			
2θ	Intensity	2θ	(hkl)	Intensity	Compound
24.971	38.394	25.057	(1 0 -2)	550.46	ZnCO ₃
31.761	637.008	31.7717	(1 0 0)	449.99	ZnO
32.441	80.272	32.5618	(1 0 4)	1000	ZnCO ₃
34.411	517.122	34.42	(0 0 2)	283.79	ZnO
36.241	1000	36.2554	(1 0 1)	1000	ZnO
47.541	199.105	47.5387	(1 0 2)	162.51	ZnO
56.581	265.137	56.5985	(2 -1 0)	272.13	ZnO
62.851	220.955	62.8538	(1 0 3)	275.02	ZnO
67.931	168.648	67.9487	(2 -1 2)	194.61	ZnO
69.071	89.682	69.0895	(2 0 1)	129.79	ZnO
		69.2117	(2 -1 9)	10.43	ZnCO ₃

4.2.2. Crystalline size

4.2.2.1. Iron oxides crystallite size distribution

The particle sizes of ilmenite and magnesioferrite were determined from the X-ray powder diffraction before and after the CO₂ adsorption test, as shown in **Figure 19** and **Figure 20**. Five crystallographic planes were used to analyze the change in the size of

both oxides present in the sample from the Ecuadorian sand. Two planes of reflection overlap in the same curve, as observed in the case of ilmenite (1 0 0), magnesioferrite (3 1 1), and the planes of ilmenite (2 0 2) and magnesioferrite (4 0 0) as presented in **Figure 19**. For magnesioferrite it was chosen the next crystallographic planes (2 2 0), (3 1 1) and (4 0 0). The size distributions of curves show a little asymmetry with a right tail, that means the largest number of crystallites are found between the peaks of these reflections. Thus, the highest point of each curve was taken to estimate a size range, which confirms the magnesioferrite has a range particle size around 30 to 120 Å. The (2 2 0) plane had the greatest density function, which means that it has many particles of this size. In case of ilmenite the selected planes were (0 1 2), (1 0 4), (1 1 0) and (2 0 2). However, the curve of (0 1 2) plane appears with a very long peak width, which means that the crystallites are distributed equitably in a great range of size around 80 to 250 Å.

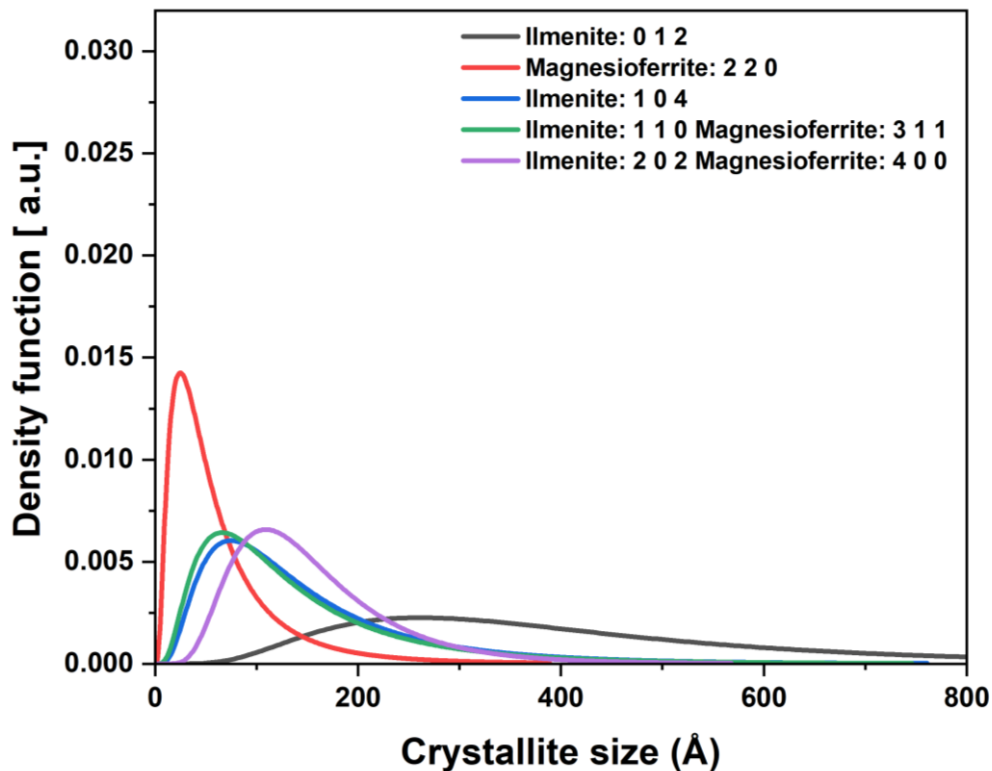


Figure 19. Crystalline size of non-reacted Iron oxides prepared at 20Hz frequency.

Then, the reacted iron oxides suffer some changes in their particle size, as seen in **Figure 20**. magnesioferrite planes (2 2 0) and (4 0 0) are shifted to the right, which means that after CO₂ test the particle size increases. The (2 2 0) peak width increases demonstrate

that sizes were more distributed around the curve than at the maximum point in comparison with the same reflection in non-reacted oxide. Therefore, the size range was changed from 60 to 180 Å. The magnesioferrite particles were aggregated or suffered a fusion of iron oxide clusters, which would lead to an increase, as shown in different studies [57]. Meanwhile, the ilmenite undergoes the opposite effect, indicating a reduction in particle size where curves tend to shift to the left. Overall, the particles in the reflection plane (0 1 2) decrease significantly in size, but the peak width becomes narrow, which means that there are many particles in a specific size. It occurs due to the disaggregation of particle clusters due to interactions with CO₂ at high pressure, leading to a reduction in size [58]. The particle density for this reflection plane is approximately 3% in relation to the other sizes, where their particle amounts are less than 1%. The other ilmenites planes (1 0 4), (1 1 0), and (2 0 2) remain equal or suffer a minimum change. Hence, the size range after exposure to the CO₂ test of ilmenite was between 10 to 180 Å.

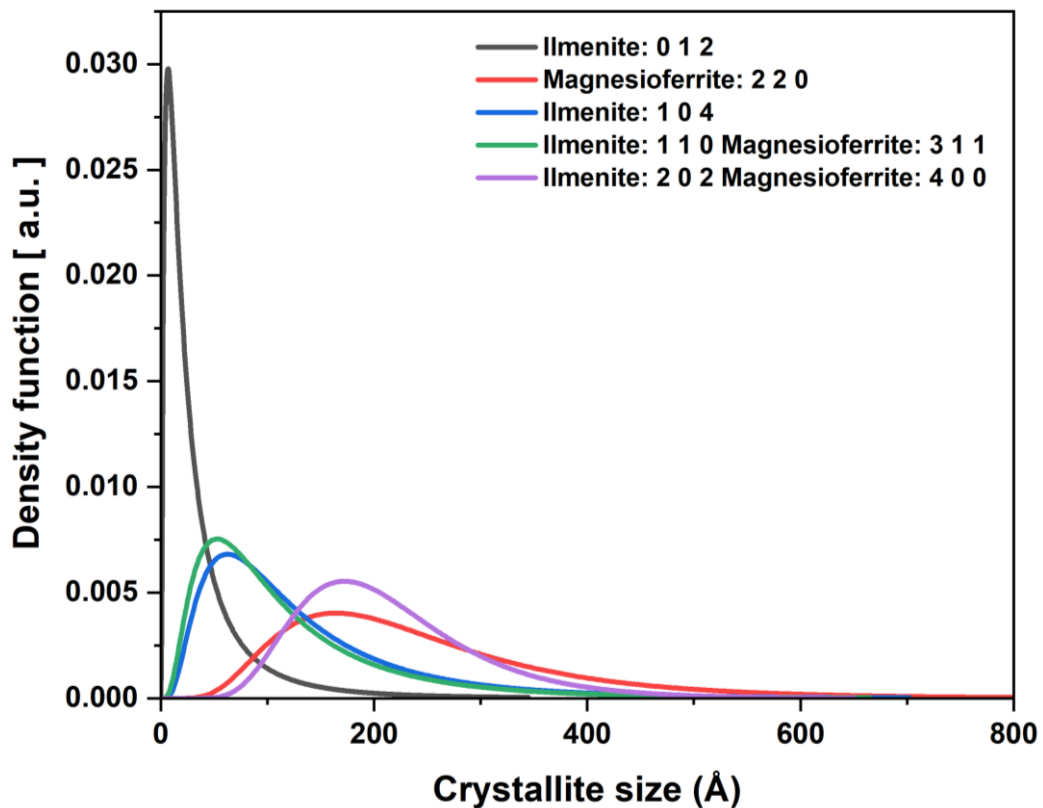


Figure 20. Crystalline size of reacted Iron oxides prepared at 20Hz frequency.

4.2.2.2. Zinc oxide crystallite size distribution

The particle size of ZnO was determined in three different steps using the experimentally acquired X-ray diffraction data. The first data were obtained after subjecting the ZnO to treatment in a milling ball at a frequency of 20 Hz, as shown in **Figure 21**. Then, three crystallographic planes are observed: (1 0 0), (0 0 2), and (1 0 1). The relative size distribution was approximately 150 and 200 Å for the planes (1 0 0) and (1 0 1), respectively. At the same time, the (0 0 2) plane increases the particle size, as it appears to peak at approximately 580 Å. The average size was calculated using the peaks of each of the curves, as in the iron oxides. These curves follow a Gaussian distribution with a right tail. Thus, the particles were in the range of 150 to 580 Å in size.

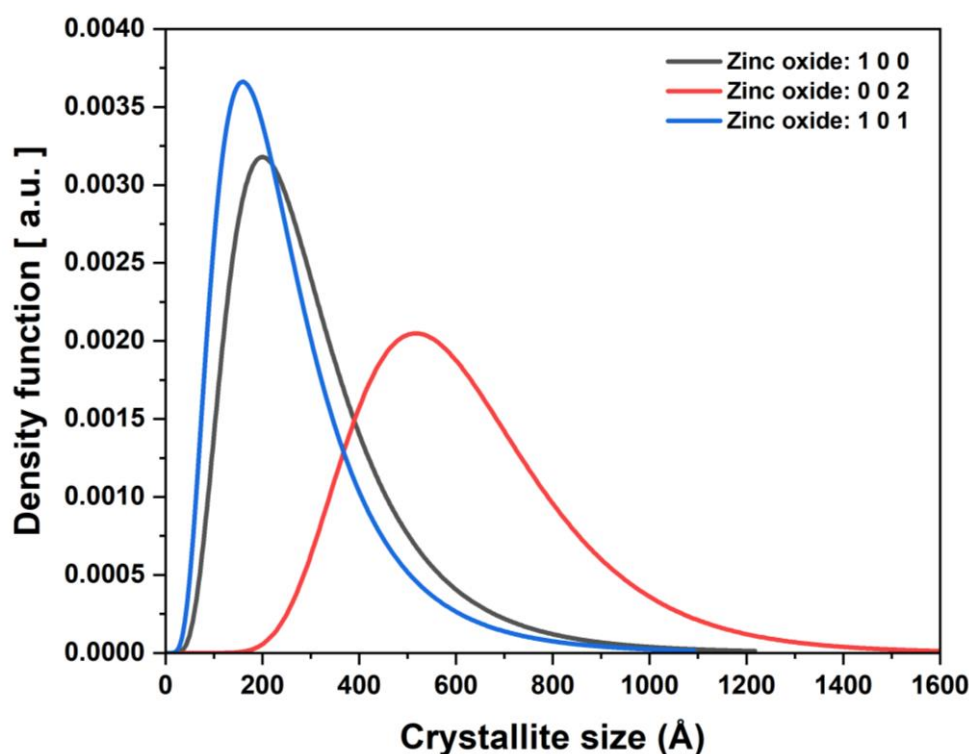


Figure 21. Crystalline size of non-reacted zinc oxide prepared at 20Hz frequency.

Meanwhile, the second data acquisition took place after conducting a CO₂ capture test on a small amount of zinc oxide. It was done to determine whether there were any structural changes, such as chemical reactions, within the material after contact with acidic gas. Therefore, an X-ray pattern was obtained for the reacted sample, and peaks

that were not present before the oxidation reaction were observed. Then, it was analyzed, and another crystalline phase composed of zinc carbonate was found. Three crystallographic planes for this new phase were selected, as shown in **Figure 22**, to compare the effect of the particle size. Subsequently, other planes with Miller indices of (0 1 2), (1 0 4), and (1 0 0) corresponding to zinc carbonate were selected; they had an average size range from 5 to 300 Å.

In contrast with **Figure 21**, the particle size of ZnO decreased significantly, and the density of the particles increased considerably. This was the result of fractionating the aggregates of the zinc oxide particles because the high pressures and the chemical interaction between the gas and oxide caused the decrease in size [59]. The initial ZnO is chemically transformed into carbonate, as seen in some research [59][60]. Thus, the new range of size for ZnO was around 10 to 30 Å.

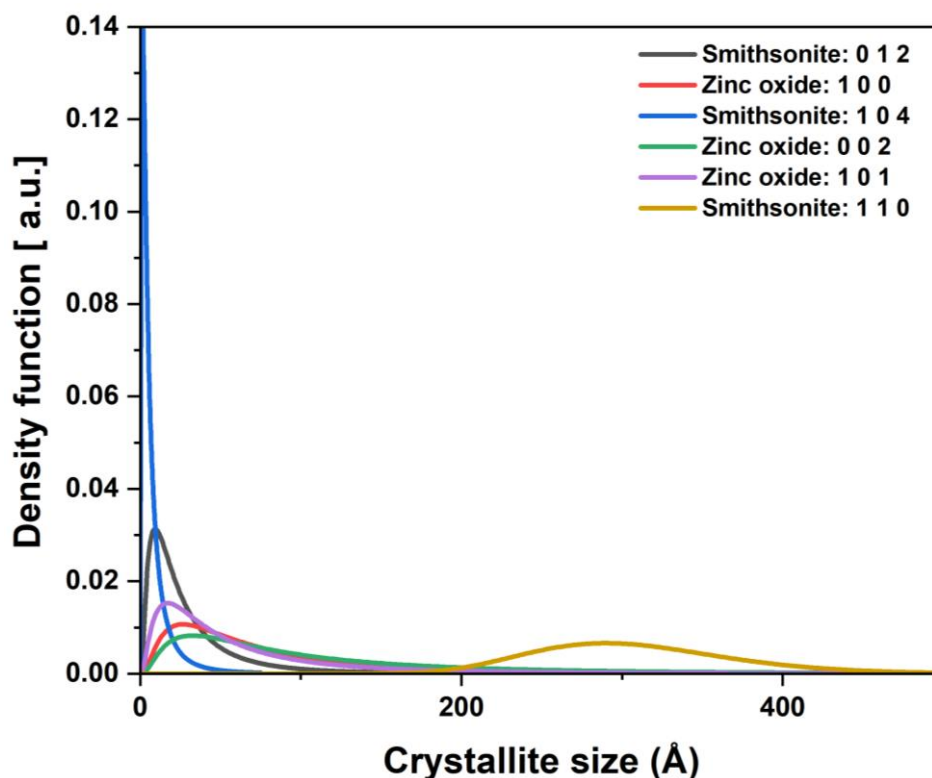


Figure 22. Crystalline size of reacted zinc oxide prepared at 20Hz frequency.

After analyzing the TGA results of the reacted sample, the temperature at which zinc carbonate decomposed ranged from 268°C to 303.4°C, as described in section 3.2.4.2. Therefore, the carbonated samples were subjected to temperatures higher than 300°C. The

sample was recovered into oxide using a muffle furnace to reach this temperature. After the recovery treatment, a diffraction pattern was obtained, as shown in **Figure 23**. Analyzing the XRD was noted that the carbonate phase completely disappeared because the crystallographic planes observed in the previous figure were no longer present in this new pattern. In addition, the particle size was almost unaffected when compared with that in **Figure 21**. Thus, the material was recovered successfully, as seen in the three crystallographic planes (1 0 0), (0 0 2), and (1 0 1) remain equal at the beginning.

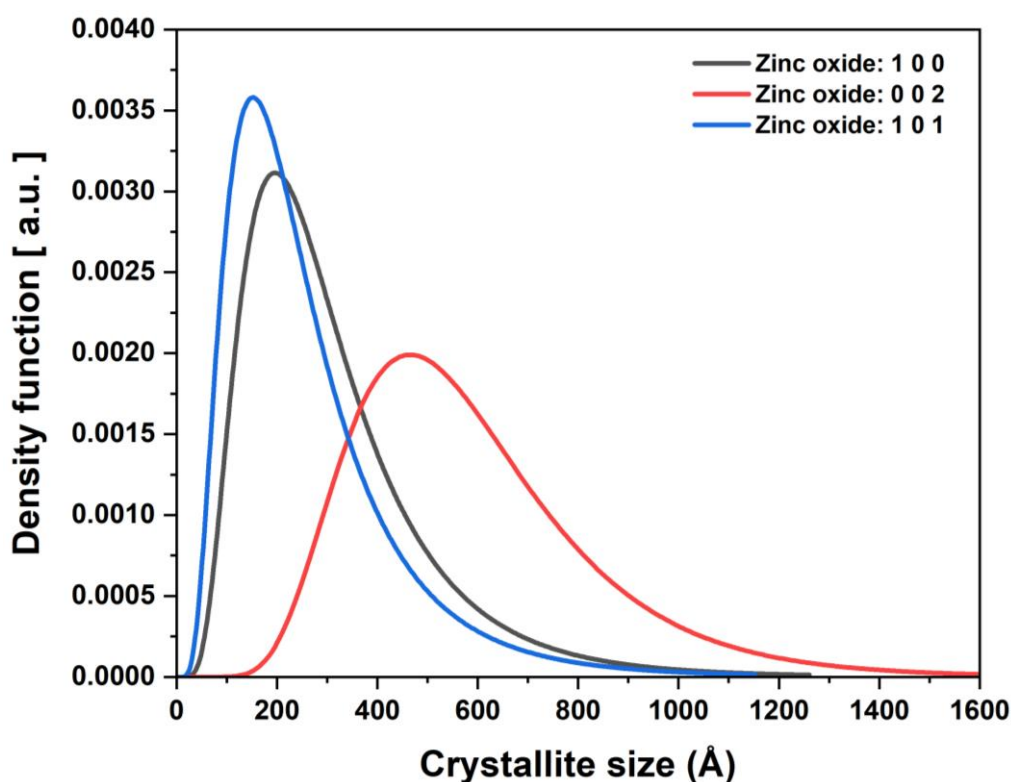


Figure 23. Crystalline size of recovered zinc oxide prepared at 20Hz frequency.

4.3. Thermogravimetric analysis (TGA)

The analysis was performed using metallic oxides after the reactivity test with CO₂ gas to determine whether there were any chemical reactions between the acidic gas and the oxides. Hence, zinc oxide and iron oxides, ilmenite, and magnesioferrite were subjected to the equipment under the conditions established in the TGA methodology. Different curves were obtained in relation to mass loss as the temperature increased. As shown in

Figure 24 the iron oxides did not suffer a loss of mass in TGA analysis. Therefore, there was no chemical reaction between CO₂ and these metallic oxides.

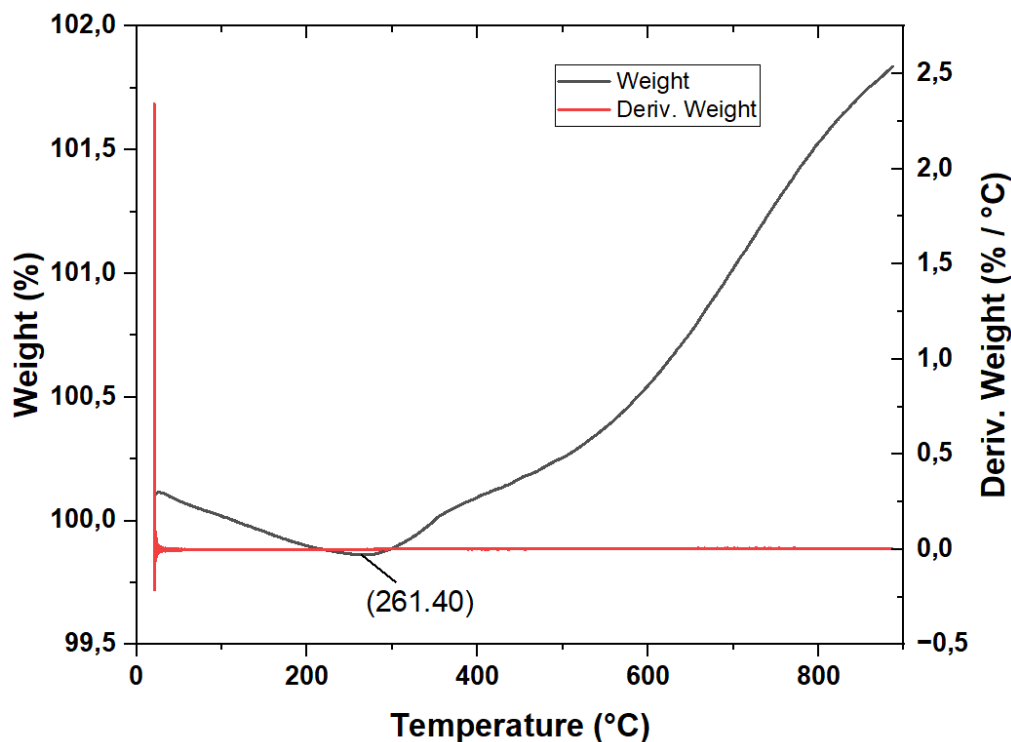


Figure 24. TGA analysis of iron oxides after reacting with CO₂ and the first derivate.

The only metal oxide that exhibited mass loss after the reaction was ZnO. Hence, it was necessary to do a deep analysis of the sample to determine the temperature of carbonate decomposition and recover the initial oxide with the help of mass loss [61]. This phase change happens because CO₂ was in contact with a metallic oxide, producing a reaction where CO₂ forms a chemical bond with the ZnO to form carbonates. Therefore, the method of sequestration is chemical adsorption. It was compared with iron oxides and CNTs, where the adsorption mechanisms occur through physical processes. Thus, the ZnO sample was reacted at 900°C and showed a mass loss of more than 13% of the initial weight. As shown in the first derivative of the TGA red curve, the temperature of decomposition starts at 260 to 310 °C. Comparing these values with other research showing decomposition ranging from 240 to 320°C was like our results [62]. It was due to the carbonate heating up to reconvert to CO₂, leaving the sample in oxide form, as shown by the black curve in **Figure 25**. Also, the theoretical decomposition of zinc carbonate involves the leaving of water that probably formed a bond with carbonates in a hydroxyl way [61].

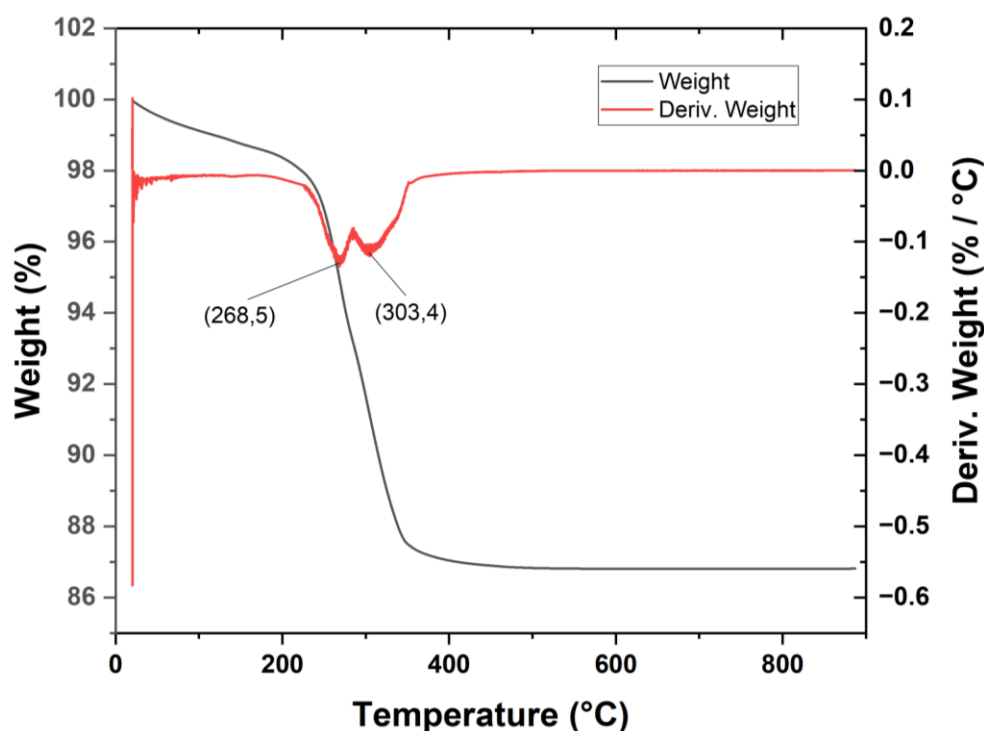


Figure 25. TGA analysis of Zinc oxide after reacting with CO₂ and the first derivate.

4.4. Porosity test

This test was performed using water as the solvent to determine the porosity of cylindrical pellets. The cylinders were weighed before and after being submerged for seven days. Then, using the dimensions of each pellet, the volume was determined to calculate the percentage of relative porosity using the dry and wet volumes, as detailed in **Table 10**. Hence, it was observed that the porosity of all the COL-307 composites was within the range of 20 to 30%. Nevertheless, the reported values of porosity typically found in kaolinite clay are around 40 to 60% of the entire volume of the membrane [63]. Therefore, the porosity values of our clay are below the average that has been analyzed in other studies. This result appears because there was an intercalation in the interlayer clay sites of guest materials, which in this research were metallic oxides and CNTs, as suggested in some works [64] [65]. This physicochemical characteristic is named pillaring, which consists of the stabilization of oxide nanoparticles, preventing aggregation through interaction with the layers [65].

Analyzing the results of porosity in detail, it was determined that the least porous pellets were made solely from COL-307 and doped with a weight percentage of 1% zinc oxide. It occurs because there was an aggregation of some ZnO particles that reduces the pores in the entire structure [66]. On the other hand, the composites with the highest porosity are those of COL-307, which contain both metallic oxides at 0.5% and CNTs at 0.01% by weight, and COL-307, which contains zinc and iron oxides at 1% by weight. These have a relative porosity percentage of 30.71% and 29.20%, as it shown in the **¡Error! No se encuentra el origen de la referencia.** with their respective standard deviations. Besides, the water retention capacity of all pellets had range among 27.5% to 31%. Therefore, it was not shown that a significant change in the absorption of water was observed in terms of whether the concentrations of carbon oxides or carbon nanotubes within the pellets varied.

Table 10. Pellets porosity test data with samples immersed in distilled water after 7 days.

Porosity Test						
Pellet-Code	Dry weight (g)	Wet weight (g)	Dry Volume (cm ³)	Wet Volume (cm ³)	Porosity (%)	Water Retention Capacity (%)
COL-307-Pure	1.5944	2.0915	1.0826	1.41989	23.7547	31.1778
COL-307-Pure-ZnO-20Hz-1%	1.5215	1.9407	1.0583	1.34986	21.5993	27.5517
COL-307-Pure-FeO-20Hz-1%	1.5331	1.9622	1.0522	1.34671	27.9899	27.9890
COL-307-Pure-CNTs-0.01%	1.553	1.9814	1.0705	1.36574	27.5796	27.5853
COL-307-Pure-ZnO and FeO-20Hz-1%	1.5956	2.0558	1.0403	1.34409	29.2022	28.8418
COL-307-Pure-ZnO-20Hz-1% and CNTs-0.01%	1.4956	1.9177	1.0765	1.38037	28.2276	28.2227
COL-307-Pure-FeO-20Hz-1% and CNTs-0.01%	1.5275	1.9561	1.0463	1.33983	28.0541	28.0589
COL-307-Pure-ZnO and FeO-20Hz-0.5% and CNTs-0.01%	1.4738	1.9264	1.0765	1.40709	30.7097	30.7097

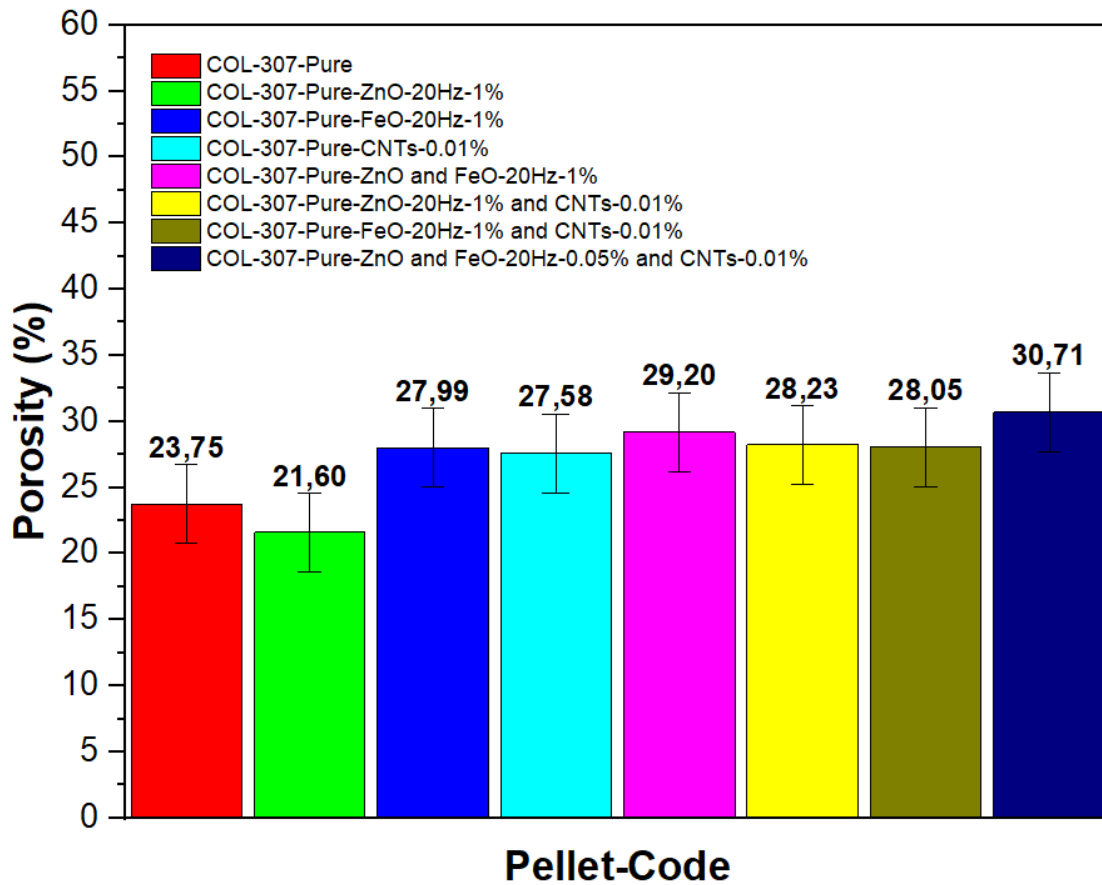


Figure 26. Porosity percentage of COL- 307 clay with different compositions of metallic oxides and CNTs.

4.5. Reactivity or adsorption test with CO₂ gas

A certain number of spherical pellets with different compositions were exposed to CO₂ adsorption tests, as shown in **Table II**. All these tests were performed inside the reactor, confined to the gas and the material, under the conditions described in the methodology in Section 3.2.6. This pressure drop in relation to the time of data acquisition was reduced to find the relationship using the gas equation between the millimoles of CO₂ adsorbed per gram of material.

The results showed that the three pellets had a significant CO₂ adsorption in relation to the rest: COL-307 with CNTs 0.01%, COL-307 with zinc oxide 1%, and COL-307 with iron oxides 1%. This is because the pressure drops were significant in relation to the mass of each sphere. One of these three composites, COL-307 with CNTs 0.01%, exhibited the

highest adsorption power of 4.21 mmol CO₂/g. Therefore, this pellet was the most promising material for enhancing CO₂ sequestration compared to clays at different compositions of metallic oxides that have been developed in this research. This can occur because of the porosity of approximately 28% and the actual structure of the doped nanotubes within the clay, which was a good intercalation between the bidimensional layers of kaolinite clay [64]. In addition, as our system works at low temperatures of 25° C, this favors the adsorption at those conditions for CNTs having Van der Waals interactions with acidic gas [67]. Its value in mmol/g was transformed and gave the following result of 185.29 mg/g of adsorbed CO₂. Compared with another study that used CNTs, which had adsorption of 114 mg/g [68], it shows that our solid membrane material had better adsorptive power.

The other two pellets with high adsorption, COL-307 with zinc oxide 1% and COL-307 with iron oxides 1%, exhibited an adsorption value of 2.36 and 3.85 mmol/g. The clay with iron oxides improved the capture because their particles were smaller than ZnO, which gave more active sites to capture more molecules of CO₂, and the mechanism of sequestration was physisorption [67]. In comparison with the clay with ZnO, where the mechanism of adsorption was by chemisorption [69] confirmed by TGA and XRD analysis, the new phase of zinc carbonate appears, as it was described in Sections 4.2 and 4.3. Also, the size of ZnO particles was larger than that of iron oxides, which decreased the number of active sites to react with CO₂.

Meanwhile, the other three composites have a rather low adsorption power of CO₂ in relation to the mass of each sphere. These composites contain carbon nanotubes in addition to one or more metal oxides incorporated within their final composition, as shown in the lower part of **Table 11**. It has an adsorptive power between 1.12 and 0.9 millimoles of CO₂ per gram of material. Also, the clay COL-307 pure pellet has an interesting average adsorptive power of 1.96 millimoles of CO₂/g since it is in the middle between the lowest and highest adsorptive power pellets. The pure clay has a medium adsorptive power due to the there was not metallic oxides in the interstices in the bidimensional layer [64]. Thus, the CO₂ gas had more active sites and great surface area to CO₂ adhere.

Table 11. Reactivity test data acquired by spherical pellets after 24 hours.

Reactivity test of spherical pellets				
Code sample	Initial weight (g)	Final weight (g)	Pressure drops (psi)	Adsorption (millimole's of CO₂/g)
COL-307-Pure	5.312	5.325	25	1.9688
COL-307-Pure-ZnO-20Hz-1%	3.3098	3.3217	23	2.3694
COL-307-Pure-FeO-20Hz-1%	3.2325	3.2597	28	3.8475
COL-307-Pure-CNTs-0.01%	3.3665	3.3832	32	4.2102
COL-307-Pure-ZnO and FeO-20Hz-1%	3.4543	3.456	10	1.3019
COL-307-Pure-ZnO-20Hz-1% and CNTs-0.01%	3.3746	3.3752	7	1.1227
COL-307-Pure-FeO-20Hz-1% and CNTs-0.01%	3.4829	3.4832	7	0.9042
COL-307-Pure-ZnO and FeO-20Hz-0.05% and CNTs-0.01%	4.2993	4.3128	8	1.0398

Chapter 5

5. Conclusion

In summary, different composites were designed with purified clay, metallic oxides, and CNTs, which allowed to determine the efficiency of CO₂ capture test of these systems. Besides, the important role of working with a purified clay phase was analyzed using XRD. It was shown that the raw clay had a high quartz content that would totally change the composition and porosity of the pellets. However, after the purification process described in this research, the purified clay was composed of kaolinite crystalline phase, which had a porous structure to the membrane. Therefore, three composites show the best adsorption power: COL-307 pure with CNTs at 0.01%, COL-307 with ZnO 1%, and COL-307 with iron oxides at 1%.

The composite that showed the best characteristics for CO₂ capture per gram of purified clay was COL-307 pure with CNTs at 0.01% of weight, in contrast with the others. Therefore, the other composites adsorb a representative quantity of acidic gas, but no more than clay doped with only CNTs, because of the process of capture arising from physical adsorption in comparison with COL-307 with ZnO 1% where the adsorption mechanism occurs by chemisorption. This occurred because of the homogenization with CNT and clay, which was performed using a sounder in a solution with distilled water, in comparison with the preparation of other pellets that were performed using mechanical stirring with a mortar. In addition, there were correct structural arrangements of CNTs inside the octahedral and tetrahedral layers of clays, which provides more surface area. This high surface area helps to sequester more molecules of CO₂ than other materials, such as metallic oxides used to create another kind of composite.

In addition, the porosity of approximately 28% of the relative porosity average of the clays plays an important role, which allows the CO₂ molecules to penetrate the entire pellet. This crystalline structure allows the gas to penetrate better inside the material and enter contact with the adsorbates. Therefore, the crystalline structure of kaolinite, which was the major phase in the clays, as well as the large surface area of the carbon nanotubes and their small particle size, interacted to obtain a material with the best physicochemical characteristics compared to the other composites to adsorb CO₂ within its structure without any physical or chemical changes that alter the composition of our material.

References

- [1] A. Yamasaki, "An overview of CO₂ mitigation options for global warming - Emphasizing CO₂ sequestration options," *Journal of Chemical Engineering of Japan*, vol. 36, no. 4, 2003, doi: 10.1252/jcej.36.361.
- [2] N. Chouikhi *et al.*, "CO₂ adsorption of materials synthesized from clay minerals: A review," *Minerals*, vol. 9, no. 9, 2019, doi: 10.3390/min9090514.
- [3] H. Yang *et al.*, "Progress in carbon dioxide separation and capture: A review," *Journal of Environmental Sciences*, vol. 20, no. 1, 2008, doi: 10.1016/S1001-0742(08)60002-9.
- [4] M. F. Brigatti, E. Galan, and B. K. G. Theng, "Chapter 2 Structures and Mineralogy of Clay Minerals," 2006. doi: 10.1016/S1572-4352(05)01002-0.
- [5] P. Bains, P. Psarras, and J. Wilcox, "CO₂ capture from the industry sector," 2017. doi: 10.1016/j.peccs.2017.07.001.
- [6] M. Olivares-Marín and M. M. Maroto-Valer, "Development of adsorbents for CO₂ capture from waste materials: A review," 2012. doi: 10.1002/ghg.45.
- [7] B. Rahmatmand, P. Keshavarz, and S. Ayatollahi, "Study of Absorption Enhancement of CO₂ by SiO₂, Al₂O₃, CNT, and Fe₃O₄ Nanoparticles in Water and Amine Solutions," *J Chem Eng Data*, vol. 61, no. 4, 2016, doi: 10.1021/acs.jced.5b00442.
- [8] F. A. Rahman *et al.*, "Pollution to solution: Capture and sequestration of carbon dioxide (CO₂) and its utilization as a renewable energy source for a sustainable future," 2017. doi: 10.1016/j.rser.2017.01.011.
- [9] R. Wennersten, Q. Sun, and H. Li, "The future potential for Carbon Capture and Storage in climate change mitigation - An overview from perspectives of technology, economy and risk," *J Clean Prod*, vol. 103, 2015, doi: 10.1016/j.jclepro.2014.09.023.
- [10] J. Rockström *et al.*, "A safe operating space for humanity," 2009. doi: 10.1038/461472a.

- [11] M. Meinshausen *et al.*, “Greenhouse-gas emission targets for limiting global warming to 2°C,” *Nature*, vol. 458, no. 7242, 2009, doi: 10.1038/nature08017.
- [12] O. A. Odunlami, D. A. Vershima, T. E. Oladimeji, S. Nkongho, S. K. Ogunlade, and B. S. Fakinle, “Advanced techniques for the capturing and separation of CO₂ – A review,” 2022. doi: 10.1016/j.rineng.2022.100512.
- [13] P. Madejski, K. Chmiel, N. Subramanian, and T. Kuś, “Methods and Techniques for CO₂ Capture: Review of Potential Solutions and Applications in Modern Energy Technologies,” 2022. doi: 10.3390/en15030887.
- [14] W. L. Theo, J. S. Lim, H. Hashim, A. A. Mustaffa, and W. S. Ho, “Review of pre-combustion capture and ionic liquid in carbon capture and storage,” 2016. doi: 10.1016/j.apenergy.2016.09.103.
- [15] A. G. Olabi *et al.*, “Assessment of the pre-combustion carbon capture contribution into sustainable development goals SDGs using novel indicators,” *Renewable and Sustainable Energy Reviews*, vol. 153, 2022, doi: 10.1016/j.rser.2021.111710.
- [16] F. Wu, P. A. Dellenback, and M. Fan, “Highly efficient and stable calcium looping based pre-combustion CO₂ capture for high-purity H₂ production,” *Mater Today Energy*, vol. 13, 2019, doi: 10.1016/j.mtener.2019.05.013.
- [17] C. A. Grande, R. Blom, K. A. Andreassen, and R. E. Stensrød, “Experimental Results of Pressure Swing Adsorption (PSA) for Pre-combustion CO₂ Capture with Metal Organic Frameworks,” in *Energy Procedia*, 2017. doi: 10.1016/j.egypro.2017.03.1364.
- [18] Y. Wang, L. Zhao, A. Otto, M. Robinius, and D. Stolten, “A Review of Post-combustion CO₂ Capture Technologies from Coal-fired Power Plants,” in *Energy Procedia*, 2017. doi: 10.1016/j.egypro.2017.03.1209.
- [19] N. S. Sifat and Y. Haseli, “A critical review of CO₂ capture technologies and prospects for clean power generation,” 2019. doi: 10.3390/en12214143.

- [20] D. Berstad, R. Anantharaman, and P. Neksa, "Low-temperature CCS from an IGCC power plant and comparison with physical solvents," in *Energy Procedia*, 2013. doi: 10.1016/j.egypro.2013.06.100.
- [21] P. Tilak and M. M. El-Halwagi, "Process integration of Calcium Looping with industrial plants for monetizing CO₂ into value-added products," *Carbon Resources Conversion*, vol. 1, no. 2, 2018, doi: 10.1016/j.crcon.2018.07.004.
- [22] S. Seepana and S. Jayanti, "Steam-moderated oxy-fuel combustion," *Energy Convers Manag*, vol. 51, no. 10, 2010, doi: 10.1016/j.enconman.2010.02.031.
- [23] T. Wall *et al.*, "An overview on oxyfuel coal combustion-State of the art research and technology development," *Chemical Engineering Research and Design*, vol. 87, no. 8, 2009, doi: 10.1016/j.cherd.2009.02.005.
- [24] Z. Zhang, T. N. Borhani, and A. G. Olabi, "Status and perspective of CO₂ absorption process," *Energy*, vol. 205, 2020, doi: 10.1016/j.energy.2020.118057.
- [25] I. P. Koronaki, L. Prentza, and V. Papaefthimiou, "Modeling of CO₂ capture via chemical absorption processes - An extensive literature review," 2015. doi: 10.1016/j.rser.2015.04.124.
- [26] J. de Riva, J. Suarez-Reyes, D. Moreno, I. Díaz, V. Ferro, and J. Palomar, "Ionic liquids for post-combustion CO₂ capture by physical absorption: Thermodynamic, kinetic and process analysis," *International Journal of Greenhouse Gas Control*, vol. 61, 2017, doi: 10.1016/j.ijggc.2017.03.019.
- [27] C. H. Yu, C. H. Huang, and C. S. Tan, "A review of CO₂ capture by absorption and adsorption," 2012. doi: 10.4209/aaqr.2012.05.0132.
- [28] P. Markewitz *et al.*, "Worldwide innovations in the development of carbon capture technologies and the utilization of CO₂," 2012. doi: 10.1039/c2ee03403d.
- [29] P. A. Webley, "Adsorption technology for CO₂ separation and capture: A perspective," *Adsorption*, vol. 20, no. 2–3, 2014, doi: 10.1007/s10450-014-9603-2.

- [30] A. L. Chaffee, G. P. Knowles, Z. Liang, J. Zhang, P. Xiao, and P. A. Webley, "CO₂ capture by adsorption: Materials and process development," *International Journal of Greenhouse Gas Control*, vol. 1, no. 1, 2007, doi: 10.1016/S1750-5836(07)00031-X.
- [31] F. Bergaya and G. Lagaly, "Chapter 1 General Introduction: Clays, Clay Minerals, and Clay Science," 2006. doi: 10.1016/S1572-4352(05)01001-9.
- [32] H. H. Murray, "Chapter 2 Structure and Composition of the Clay Minerals and their Physical and Chemical Properties," 2006. doi: 10.1016/S1572-4352(06)02002-2.
- [33] X. Tan, F. Liu, L. Hu, A. H. Reed, Y. Furukawa, and G. Zhang, "Evaluation of the particle sizes of four clay minerals," *Appl Clay Sci*, vol. 135, 2017, doi: 10.1016/j.clay.2016.10.012.
- [34] M. F. Brigatti, E. Galán, and B. K. G. Theng, "Structure and Mineralogy of Clay Minerals," in *Developments in Clay Science*, vol. 5, 2013. doi: 10.1016/B978-0-08-098258-8.00002-X.
- [35] L. J. Michot and F. Villiéras, "Chapter 12.9 Surface Area and Porosity," 2006. doi: 10.1016/S1572-4352(05)01035-4.
- [36] D. Savage and J. Liu, "Water/clay ratio, clay porosity models and impacts upon clay transformations," *Appl Clay Sci*, vol. 116–117, 2015, doi: 10.1016/j.clay.2015.08.011.
- [37] G. S. Parkinson, "Iron oxide surfaces," 2016. doi: 10.1016/j.surfrep.2016.02.001.
- [38] N. C. Wilson, J. Muscat, D. Mkhonto, P. E. Ngoepe, and N. M. Harrison, "Structure and properties of ilmenite from first principles," *Phys Rev B Condens Matter Mater Phys*, vol. 71, no. 7, 2005, doi: 10.1103/PhysRevB.71.075202.
- [39] V. Ponomar, "Crystal structures and magnetic properties of spinel ferrites synthesized from natural Fe–Mg–Ca carbonates," *Mater Res Bull*, vol. 158, 2023, doi: 10.1016/j.materresbull.2022.112068.

- [40] A. J. Antone, Z. Sun, and Y. Bao, "Preparation and application of iron oxide nanoclusters," 2019. doi: 10.3390/magnetochemistry5030045.
- [41] F. Habashi, "Zinc, the metal from the east," 2002.
- [42] S. Ji and C. Ye, "Synthesis, growth mechanism, and applications of zinc oxide nanomaterials," *J Mater Sci Technol*, vol. 24, no. 4, 2008.
- [43] A. Moezzi, A. M. McDonagh, and M. B. Cortie, "Zinc oxide particles: Synthesis, properties and applications," 2012. doi: 10.1016/j.cej.2012.01.076.
- [44] Z. L. Wang, "Zinc oxide nanostructures: Growth, properties and applications," *Journal of Physics Condensed Matter*, vol. 16, no. 25, 2004, doi: 10.1088/0953-8984/16/25/R01.
- [45] O. Dulub, L. A. Boatner, and U. Diebold, "STM study of the geometric and electronic structure of ZnO(0 0 0 1)-Zn, (0 0 0 Γ)-O, (1 0 Γ 0), and (1 1 $\bar{2}$ 0) surfaces," *Surf Sci*, vol. 519, no. 3, 2002, doi: 10.1016/S0039-6028(02)02211-2.
- [46] K. S. Ibrahim, "Carbon nanotubes-properties and applications: a review," *Carbon letters*, vol. 14, no. 3, 2013, doi: 10.5714/cl.2013.14.3.131.
- [47] M. F. L. De Volder, S. H. Tawfick, R. H. Baughman, and A. J. Hart, "Carbon nanotubes: Present and future commercial applications," 2013. doi: 10.1126/science.1222453.
- [48] V. N. Popov, "Carbon nanotubes: Properties and application," 2004. doi: 10.1016/j.mser.2003.10.001.
- [49] A. Bachtold, P. Hadley, T. Nakanishi, and C. Dekker, "Logic circuits with carbon nanotube transistors," *Science (1979)*, vol. 294, no. 5545, 2001, doi: 10.1126/science.1065824.
- [50] S. Hsu and C. Lu, "Modification of single-walled carbon nanotubes for enhancing isopropyl alcohol vapor adsorption from air streams," *Sep Sci Technol*, vol. 42, no. 12, 2007, doi: 10.1080/01496390701515060.

- [51] F. Su, C. Lu, W. Cnen, H. Bai, and J. F. Hwang, "Capture of CO₂ from flue gas via multiwalled carbon nanotubes," *Science of the Total Environment*, vol. 407, no. 8, 2009, doi: 10.1016/j.scitotenv.2009.01.007.
- [52] C. Lu, H. Bai, B. Wu, F. Su, and J. F. Hwang, "Comparative study of CO₂ capture by carbon nanotubes, activated carbons, and zeolites," *Energy and Fuels*, vol. 22, no. 5, 2008, doi: 10.1021/ef8000086.
- [53] A. Altomare, C. Cuocci, C. Giacobazzo, A. Moliterni, and R. Rizzi, "QUALX: A computer program for qualitative analysis using powder diffraction data," 2008. doi: 10.1107/S0021889808016956.
- [54] A. Altomare, N. Corriero, C. Cuocci, A. Falcicchio, A. Moliterni, and R. Rizzi, "QUALX2.0: A qualitative phase analysis software using the freely available database POW-COD," *J Appl Crystallogr*, vol. 48, 2015, doi: 10.1107/S1600576715002319.
- [55] F. Bergaya and G. Lagaly, "Purification of natural clays," in *Developments in Clay Science*, vol. 5, 2013. doi: 10.1016/B978-0-08-098258-8.00008-0.
- [56] M. Valkov and G. Simha, "Vermiculite: Structural Properties and Examples of the Use," in *Clay Minerals in Nature - Their Characterization, Modification and Application*, 2012. doi: 10.5772/51237.
- [57] E. Y. Mora Mendoza *et al.*, "Iron oxides as efficient sorbents for CO₂ capture," *Journal of Materials Research and Technology*, vol. 8, no. 3, 2019, doi: 10.1016/j.jmrt.2019.05.002.
- [58] F. N. Ridha, M. A. Duchesne, X. Lu, D. Y. Lu, D. Filippou, and R. W. Hughes, "Characterization of an ilmenite ore for pressurized chemical looping combustion," *Appl Energy*, vol. 163, 2016, doi: 10.1016/j.apenergy.2015.10.070.
- [59] M. T. Dunstan, F. Donat, A. H. Bork, C. P. Grey, and C. R. Müller, "CO₂Capture at Medium to High Temperature Using Solid Oxide-Based Sorbents: Fundamental Aspects, Mechanistic Insights, and Recent Advances," 2021. doi: 10.1021/acs.chemrev.1c00100.

- [60] Z. S. Li, F. Fang, X. Y. Tang, and N. S. Cai, "Effect of temperature on the carbonation reaction of CaO with CO₂," *Energy and Fuels*, vol. 26, no. 4, 2012, doi: 10.1021/ef201543n.
- [61] A. Barhoum *et al.*, "Synthesis, growth mechanism, and photocatalytic activity of Zinc oxide nanostructures: porous microparticles versus nonporous nanoparticles," *J Mater Sci*, vol. 52, no. 5, 2017, doi: 10.1007/s10853-016-0567-3.
- [62] N. Kanari, D. Mishra, I. Gaballah, and B. Dupré, "Thermal decomposition of zinc carbonate hydroxide," *Thermochim Acta*, vol. 410, no. 1–2, 2004, doi: 10.1016/S0040-6031(03)00396-4.
- [63] S. Li and N. Li, "Effects of composition and temperature on porosity and pore size distribution of porous ceramics prepared from Al(OH)₃ and kaolinite gangue," *Ceram Int*, vol. 33, no. 4, 2007, doi: 10.1016/j.ceramint.2005.11.004.
- [64] K. G. Bhattacharyya and S. Sen Gupta, "Adsorption of a few heavy metals on natural and modified kaolinite and montmorillonite: A review," 2008. doi: 10.1016/j.cis.2007.12.008.
- [65] R. A. Schoonheydt, T. Pinnavaia, G. Lagaly, and N. Gangas, "Pillared clays and pillared layered solids (Technical Report)," *Pure and Applied Chemistry*, vol. 71, no. 12, 1999, doi: 10.1351/pac199971122367.
- [66] C. W. Chang, Y. H. Kao, P. H. Shen, P. C. Kang, and C. Y. Wang, "Nanoconfinement of metal oxide MgO and ZnO in zeolitic imidazolate framework ZIF-8 for CO₂ adsorption and regeneration," *J Hazard Mater*, vol. 400, 2020, doi: 10.1016/j.jhazmat.2020.122974.
- [67] M. Cinke, J. Li, C. W. Bauschlicher, A. Ricca, and M. Meyyappan, "CO₂ adsorption in single-walled carbon nanotubes," *Chem Phys Lett*, vol. 376, no. 5–6, 2003, doi: 10.1016/S0009-2614(03)01124-2.
- [68] S. C. Hsu, C. Lu, F. Su, W. Zeng, and W. Chen, "Thermodynamics and regeneration studies of CO₂ adsorption on multiwalled carbon nanotubes," *Chem Eng Sci*, vol. 65, no. 4, 2010, doi: 10.1016/j.ces.2009.10.005.

- [69] G. S. Rao *et al.*, “Adsorption mechanism of graphene-like ZnO monolayer towards CO₂ molecules: Enhanced CO₂ capture,” *Nanotechnology*, vol. 27, no. 1, 2015, doi: 10.1088/0957-4484/27/1/015502.